UCLouvain

epl

École polytechnique de Louvain

# Design of a passive abduction/adduction degree-of-freedom for a hip prosthesis

Author: **Hugo Duvivier**
Supervisor: **Renaud Ronsse**
Readers: **Louis Devillez, Benoît Herman**
Academic year 2024–2025
Master [120] in Mechanical Engineering

# Abstract

Among lower-limb amputations, hip disarticulation and hemipelvectomy are the most extreme, posing significant challenges for prosthetic development. These types of amputations are relatively rare, which slows down research progress in the field of hip joint prostheses. Although several hip disarticulation prostheses exist, both commercial and experimental, only a few incorporate motion in the frontal plane, and those that do are exclusively active systems. The lack of a solution to assist the prosthetic leg in performing abduction/adduction during gait means that users must rely on their own bodies to stabilize themselves in the frontal plane while walking, increasing their energy expenditure. This master thesis aims to address this gap by implementing a passive abduction/adduction degree of freedom on an existing hip prosthesis. The actuation is achieved using springs, which store and release energy to allow motion in the frontal plane without active control. Determining the stiffness of the hip in the frontal plane and selecting suitable springs are key steps of this work. The proposed degree of freedom is integrated into the base of the existing prosthesis and consists of an upper and lower part connected by a shaft, allowing controlled rotation in the frontal plane. The design prioritizes compactness in order to preserve the main characteristics of the original prosthesis. A 3D-printed prototype has been assembled, and a complete test protocol has been developed to validate its performance, awaiting future experimental execution.

# Acknowledgements

I would like to sincerely thank everyone who has supported and guided me throughout the completion of this thesis.

Firstly, I want to thank my parents who supported me and guided me throughout my academic career and during this work which is the final touch of this fulfilling journey.

I am deeply grateful to Valentine who heard about all the details of this work all the process long. Thank you for your patience and your wise advice.

Thank you to my friends Loïc and Victor who have proofread my work. A special thanks to Victor for the spelling and grammar correction.

I would also like to thank Benoît Herman for agreeing to read my work as a member of my jury.

I am deeply grateful to my supervisor, Renaud Ronsse, for the guidance and valuable advice throughout this work.

Finally, I wish to express my deepest and heartfelt gratitude to Louis Devillez without whom this thesis would not have been possible. Thank you for your time, your advices, the enriching exchanges we had during this last year and the guidance from the beginning to the end.

# Contents

# Chapter 1

# Introduction

## 1.1 Motivation

Hip disarticulation and hemipelvectomy are two major surgical procedures involving the removal of the entire lower limb, but with different extents. In a hip disarticulation, the amputation is performed through the hip joint, completely removing the femur while preserving the pelvic bones. In a hemipelvectomy, however, a part or half of the pelvis is removed. In 2006, the number of such procedures in the Netherlands was approximately 40, representing about 1.3 % of all lower limb amputations [1].

The most common cause of these amputations is tumor [2–6], although they can also result from severe injuries or trauma.

Because both procedures remove the hip joint, they also result in the loss of the knee and ankle joints, creating major rehabilitation challenges and increasing the energy required for walking or performing daily activities [7].

To restore independence, research efforts worldwide focus on designing prostheses for these specific amputations. While knee and ankle prostheses are well-established for transtibial or transfemoral amputations, hip joint prostheses are exclusively suited for hemipelvectomy or hip disarticulation. These three prosthetic joints must function together to reproduce, as closely as possible, the gait of a healthy person.

Patients also require a custom-made socket in which there is a lamination plate to attach the prosthesis. Modern sockets are molded from composite materials to match the patient's body shape, as shown in Figures 1.10 and 1.12.

Walking stability depends on balance control in both the sagittal and frontal planes (Figure 1.3) [8]. Stability in the sagittal plane requires active motor control, while in the frontal plane it can be achieved through passive body dynamics but maintaining it demands constant energy from the user. Adding a passive abduction/adduction degree of freedom to a hip prosthesis could reduce this energy cost, allowing users to walk longer distances with greater autonomy.

One key design challenge is keeping the prosthesis compact and lightweight. A heavier device requires larger motors, which in turn increase weight. By implementing this degree of freedom passively, the mechanism can remain light and simple, offering unlimited battery autonomy and reduced cost.

## 1.2 Biomechanics of the hip joint during walking gait

Before discussing prostheses, it is crucial to understand the underlying problem this thesis aims to address. Since the goal is to design a passive degree of freedom for a hip disarticulation prosthesis that helps disabled people walk, the first step is to describe the walking gait cycle. To clearly present the concepts and challenges involved, this section focuses on the biomechanics of the hip joint in the frontal plane during gait. For brevity, the term gait will refer exclusively to walking gait throughout the thesis.

### 1.2.1 The walking gait cycle

Walking is a daily activity that follows a repetitive sequence called the gait cycle. For a single leg, this cycle is divided into two main phases: the stance phase and the swing phase (Figure 1.1).

The stance phase corresponds to the period during which the foot remains in contact with the ground [9]. It begins with initial contact and ends when the foot lifts off, marking the transition to the swing phase. The swing phase, in turn, is defined as the interval when the foot is in the air to allow limb advancement [9], starting at toe-off and concluding with the next ground contact. Consequently, the gait cycle can be described as the time interval between two successive occurrences of the same walking event [9].

The stance phase is composed of five events: heel strike, loading response, mid-stance, terminal stance, and pre-swing. Heel strike and pre-swing are stages when both feet are in contact with the ground, referred to as double support in Figure 1.1. These act as transitions between the two main phases. The other events occur during single support, when only one foot touches the ground and bears the entire body weight.

The swing phase consists of three events: toe-off, mid-swing, and terminal swing. During this entire phase, the leg is not in contact with the ground and remains completely unloaded.

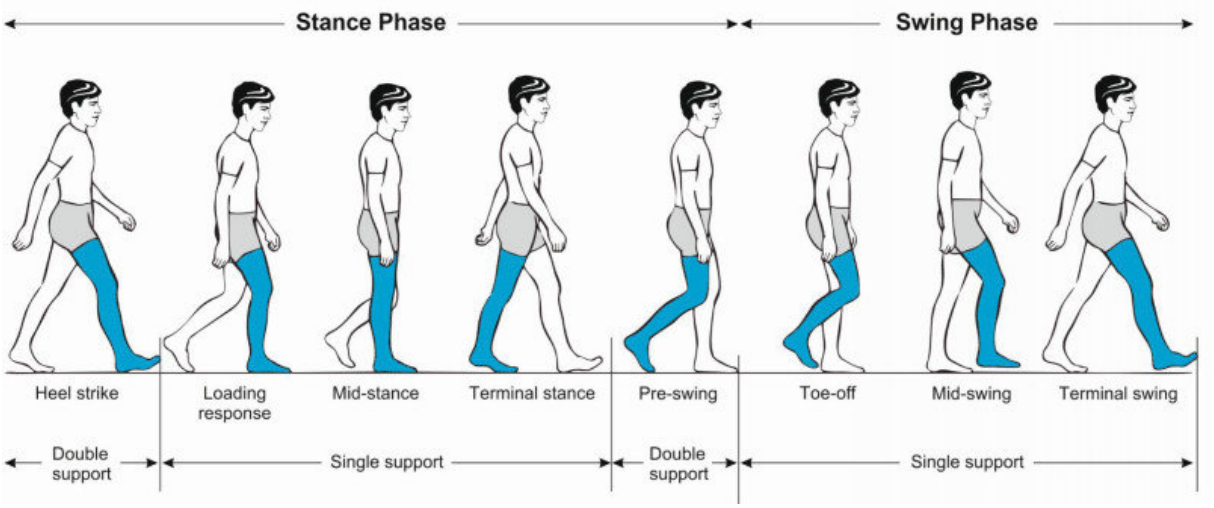


Figure 1.1: Phases of the normal gait cycle [10]

According to [11], the stance phase accounts for approximately the first 60% of the cycle, while the swing phase covers the remaining 40%.

### 1.2.2 Hip joint mechanics in the frontal plane during walking gait

The hip is a key joint in the human body, enabling the motion of the lower limbs and allowing activities such as walking, sitting, jumping, and running. It is a ball-and-socket joint that provides three degrees of freedom: external and internal rotation, adduction and abduction (Figure 1.2), and flexion and extension.

The human body can be described in three anatomical planes: transverse, sagittal, and frontal (Figure 1.3). Each of the hip's three degrees of freedom corresponds to a movement within one of these planes. External and internal rotation occur in the transverse plane, flexion and extension in the sagittal plane, and adduction and abduction in the frontal plane (also referred to as the coronal plane in some publications).

The present thesis focuses on the abduction/adduction movement, as it is the degree of freedom targeted for integration into the prosthesis.

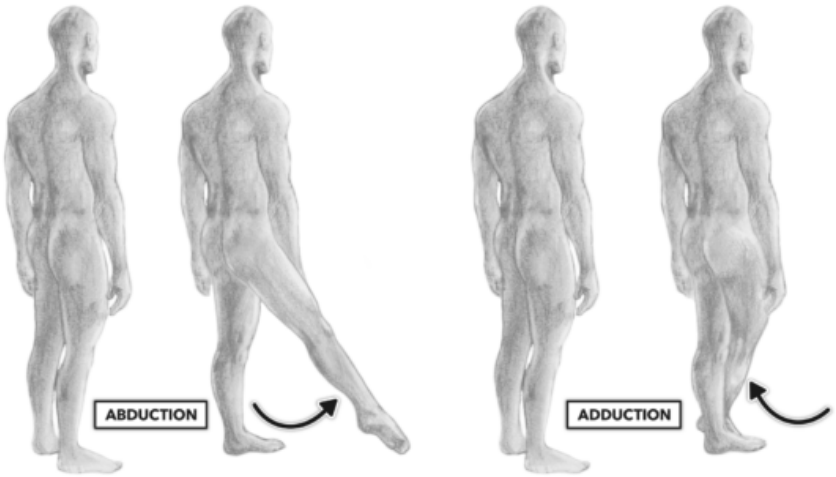


Figure 1.2: Abduction and adduction of the hip [12]

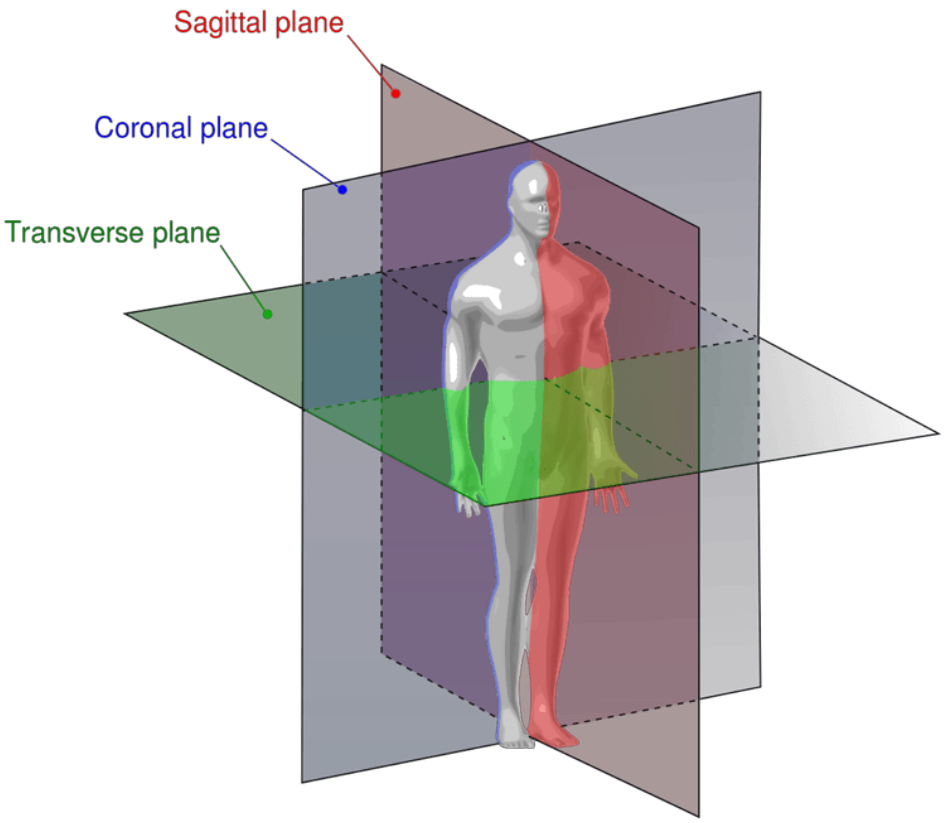


Figure 1.3: Anatomical body planes [13]

Figures 1.4 and 1.5 show the hip angle and moment in the frontal plane during a gait cycle. At the start of the cycle, during the first double support sub-phase (heel strike), the hip angle is not zero and generates a positive adduction moment. As the cycle transitions into the single support sub-phase of the stance, the hip angle reaches zero. Throughout this single support phase, the hip maintains a negative adduction moment (positive abduction) to stabilize the body, while the hip angle remains in positive adduction. Before the swing phase begins, the hip returns to the zero angle and zero moment position. During the swing phase, the hip angle remains in positive abduction, but the joint still produces a positive adduction moment to help stabilize the body. The end of the swing phase marks the completion of the gait cycle.

The range of motion of the hip in different planes is shown in Figure 1.6, with the coronal plane corresponding to the frontal plane as previously mentioned. In the frontal plane, the maximum abduction angle is approximately 10°, and the maximum adduction angle is of a similar magnitude (Figure 1.4).

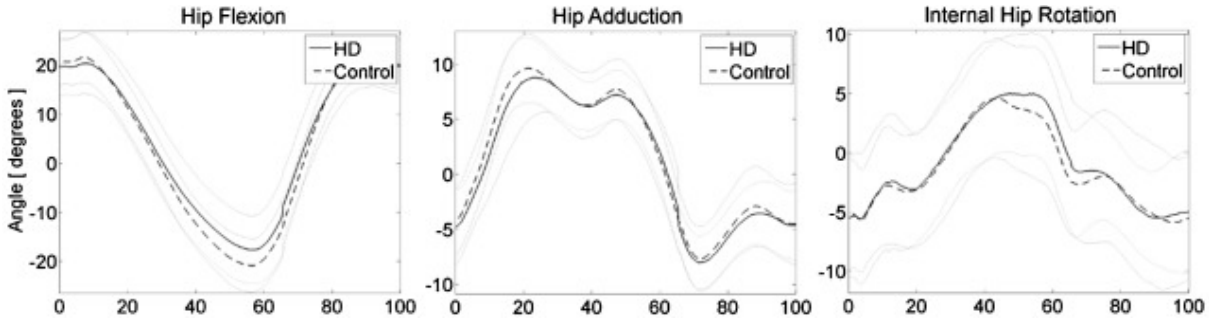


Figure 1.4: Hip angles during walking [14]. HD line represents people with hip dysplasia; control line represents a healthy control group.

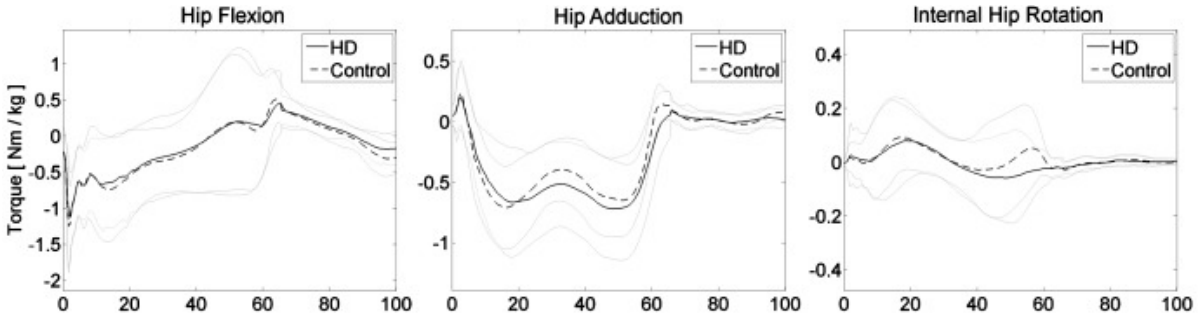


Figure 1.5: Hip moments during walking [14]. HD line represents people with hip dysplasia; control line represents a healthy control group.

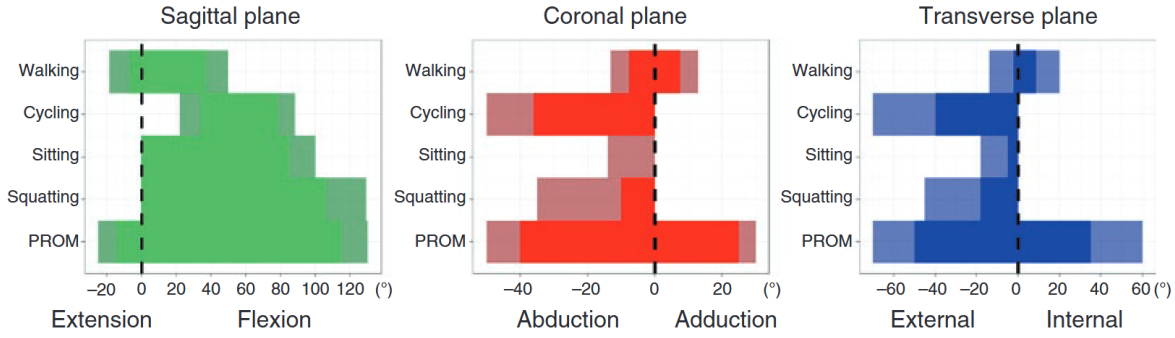


Figure 1.6: Maximum (pale) and average (bright) hip joint range of movement during PROM (passive range of movement), squatting, sitting, cycling (including mounting and dismounting), and walking. Data adapted from [11] using measurements from [15–17].

## 1.3 State of the art of the hip disarticulation prosthesis

This section presents a literature review of hip disarticulation prostheses, including both commercialized models and prototypes. It also covers ankle prostheses that implement passive frontal plane motion, to illustrate how similar challenges are addressed in this type of device.

### 1.3.1 Commercialized disarticulation hip prostheses

Before the development of the so-called Canadian prosthesis, several types of hip disarticulation prostheses were created to meet the needs of patients requiring hip replacement after the Second World War.

The first was the Saucer-type prosthesis [18], developed between 1940 and 1950. It allowed movement only in the sagittal plane (Figure 1.7). The second was the Tilting-table prosthesis (Figure 1.8), introduced in the 1950s with the aim of simulating the natural dynamics of the hip joint. It also had a single degree of freedom in the sagittal plane. During the same period, the U.S. Navy developed its own device, the U.S. Navy Hydraulic Prosthesis (Figure 1.9). Thanks to its hydraulic cylinder, it could be manually controlled and locked in any position, but still had only one degree of freedom in the sagittal plane.

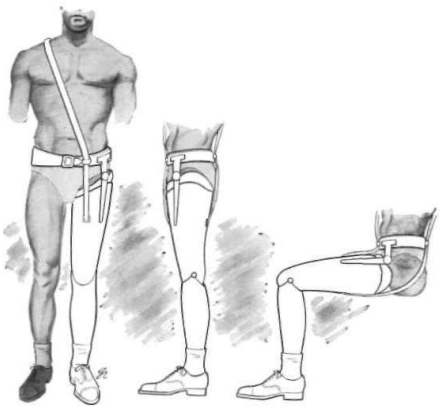

Figure 1.7: Sketch of the Saucer-type hip disarticulation prosthesis [18].

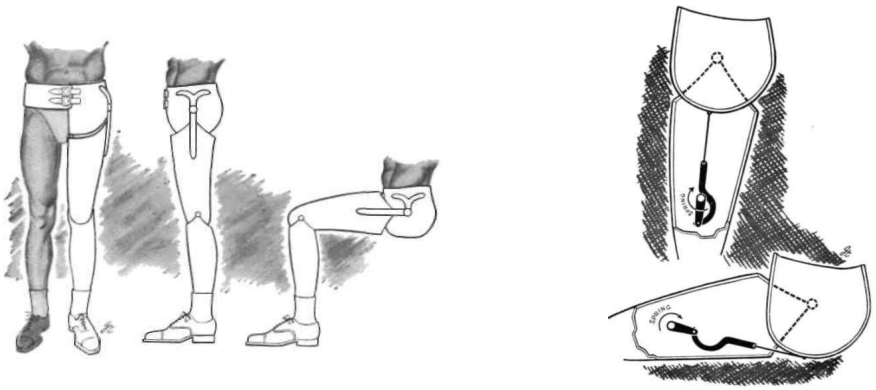

Figure 1.8: Sketch of the Tilting-table prosthesis [18]. Left : Sit and stand positions; right : standing and sitting view of the latch-type medial support.

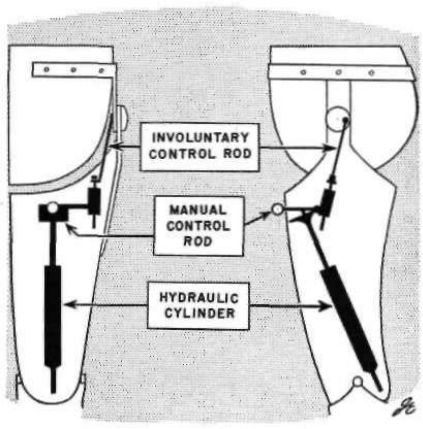


Figure 1.9: Sketch of the U.S. Navy Hydraulic Prosthesis [18].

Research on the Canadian-type hip prosthesis is considered as the first serious attempt to develop a hip disarticulation prosthesis [18]. Designed in the 1950s in Toronto, it has evolved over the years to become a reference model. Like its predecessors, it features a single degree of freedom in the sagittal plane (Figure 1.10).

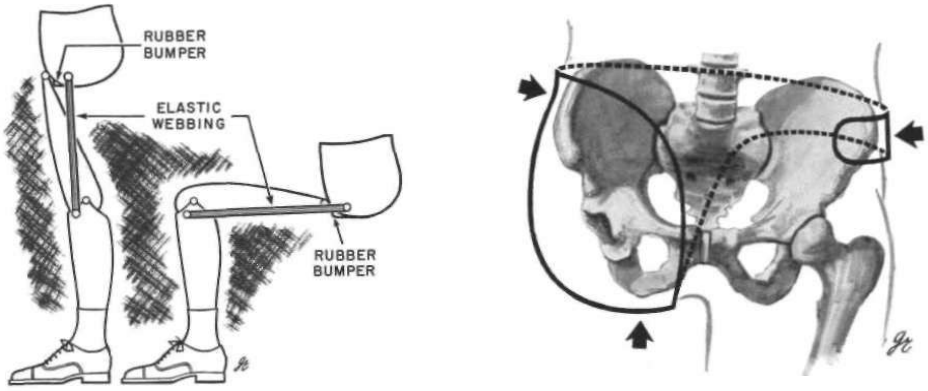


Figure 1.10: Left : Sketch of the final Canadian prosthesis; right : representation of the socket [18].

The Ottobock 3R21 and 3R30 are knee disarticulation joints that have also been used as hip joints [19] (Figure 1.11). Released around 1980, they were designed to address the hip flexion bias, meaning the prosthetic leg must be slightly shorter than the intact one to ensure foot clearance during the swing phase [20]. These devices also have a single degree of freedom in the sagittal plane.

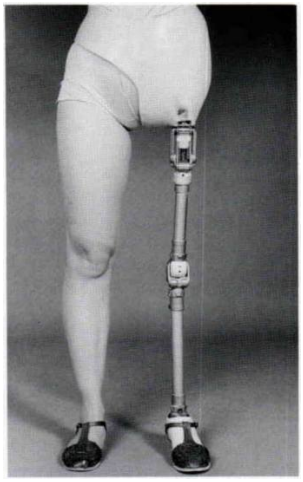

Figure 1.11: Patient using an Ottobock 3R21 as a hip prosthesis [19].

The Ottobock 7E7, introduced around 2010 (Figure 1.12), allows motion in the sagittal plane and can be adjusted in the frontal and transverse planes to fit each patient's anatomy and center of rotation.

Figure 1.12: Ottobock 7E7 prosthesis.Left : 3D rearview; middle : View of the prosthesis attached to the socket; right : closer view.

The Ottobock 7E10, also known as the "Helix 3D", was commercialized in 2019 and is one of the most advanced prosthetic hip joints currently available on the market. It shortens the leg during the swing phase to compensate for hip flexion bias, and its gait phases (swing and stance) are hydraulically controlled. While it has a degree of freedom in the sagittal plane, it can also rotate during swing to facilitate pre-swing, enabling a so-called "three-dimensional" hip movement. This rotation is not an implementation of abduction/adduction, but rather a coupling between hip flexion and rotation. The device is shown in Figure 1.13.


Figure 1.13: Ottobock 7E10 prosthesis. Left : side view; middle : 3D view; right : view of the tilt mechanism enabling "3D" movement.

### 1.3.2 Prototyped disarticulation hip-prosthesis

Several research projects worldwide have explored hip disarticulation prostheses that did not lead to commercial products.

In 2009, N. Hata, K. Tsutomu, and I. Takenobu designed a powered prosthesis capable of controlling the swing phase, with movement restricted to the sagittal plane [21]. A schematic of this design is shown in Figure 1.14.

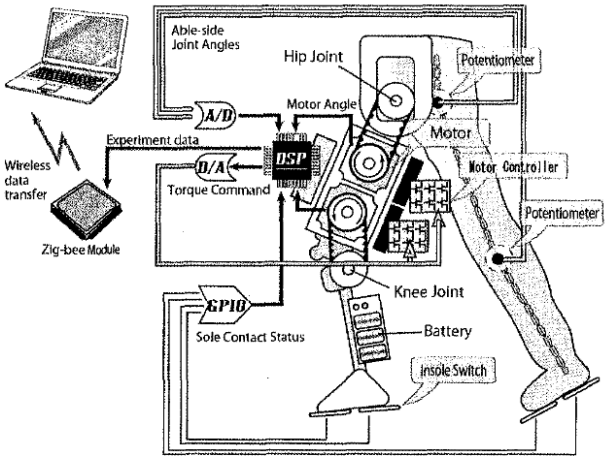


Figure 1.14: Schematic of the prosthesis (in the sagittal plane) designed by N. Hata et al. [21]

In 2015, Langlois [22] developed a powered hip prosthesis featuring two powered joints: one for sagittal plane movement and another for frontal plane rotation. The device, mounted laterally, is illustrated in Figure 1.15.

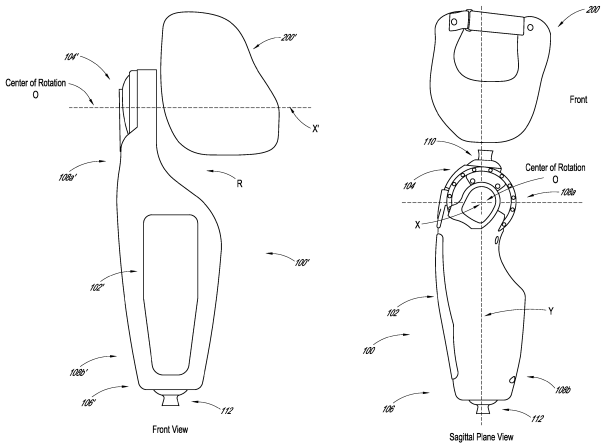


Figure 1.15: Schematic of the prosthesis designed by Langlois. Left : frontal plane view; right : sagittal plane view. [22]

A modification of the work of N. Hata and Al. [21] was proposed in 2019 by Y. Ueyama et al. [23], resulting in a powered robotic prosthesis aimed at allowing non-amputees to simulate walking with such a device for gait analysis. It only implements sagittal plane movement (Figure 1.16).

Figure 1.16: Sagittal plane view of the prosthesis designed by Y. Ueyama, mounted on an adapter for able-bodied testing. [23]

In 2023, S. Luo et al. [24] developed a powered hip prosthesis capable of adjusting its rotation center, enabling abduction/adduction with motors and achieving over 95 % motion reproduction accuracy. It also integrates a synergy mechanism with the knee prosthesis.

The same year, K. Brannen [25] presented in his master thesis at the University of Ottawa, a microprocessor-controlled powered hip prosthesis using pulleys and cables (Figure 1.17). This model lacks frontal plane motion and relies on a hip abduction orthosis for stability.

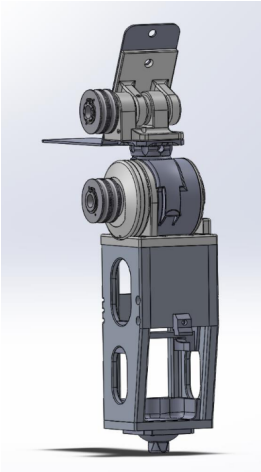

Figure 1.17: 3D CAD model of the prosthesis designed by K. Brannen. [25]

Also in 2023, S. Mroz [20] designed for her master thesis at the University of Ottawa, a laterally mounted powered prosthesis limited to sagittal plane movement, shown in Figure 1.18.

Figure 1.18: Prosthesis designed by S. Mroz. Left : 3D-printed prototype; right : frontal plane view of the final version. [20]

In 2024, L. Devillez [26] developed a compact, lightweight powered hip prosthesis using a double parallelogram mechanism for reduced volume. Limited to sagittal plane motion, this design serves as the basis for the present work (Figure 1.19).

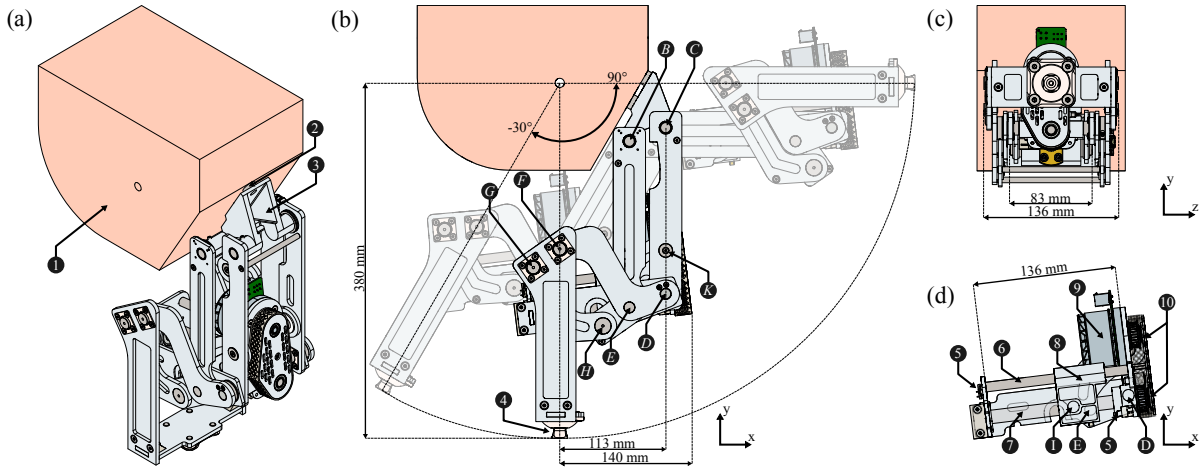


Figure 1.19: Complete CAD design of the prosthesis: (a) corner view in standing position, (b) sagittal view in standing position with extrema semi-transparent, (c) frontal view in sitting position, (d) sagittal view of transmission with front bar transparent. Numbers: ① simplified shell, ② rigid plate attachment, ③ base, ④ pyramidal adapter, ⑤ micro-switch, ⑥ guiding rails, ⑦ powerscrew, ⑧ carriage, ⑨ motor, ⑩ pulleys. Uppercase letters refer to joints. From [26]

### 1.3.3 Ankle prostheses with passive inversion/eversion

Ankle joint loss occurs in all lower-limb amputations, making it a focus of extensive research due to its prevalence compared to hip joint loss [27]. The ankle has two degrees of freedom: plantar flexion/dorsiflexion in the sagittal plane and inversion/eversion in the frontal plane. The latter is of interest here, as it represents frontal plane motion similar to the aim of this thesis.

This subsection provides a brief review of ankle prostheses that incorporate passive inversion/eversion, to assess solutions developed for other lower-limb joints.

In 2022, the Lovely Professional University (India) presented a passive ankle-foot prosthesis with inversion-eversion assisted by dampers on each side (Figure 1.20) [28]. This device remains a prototype.

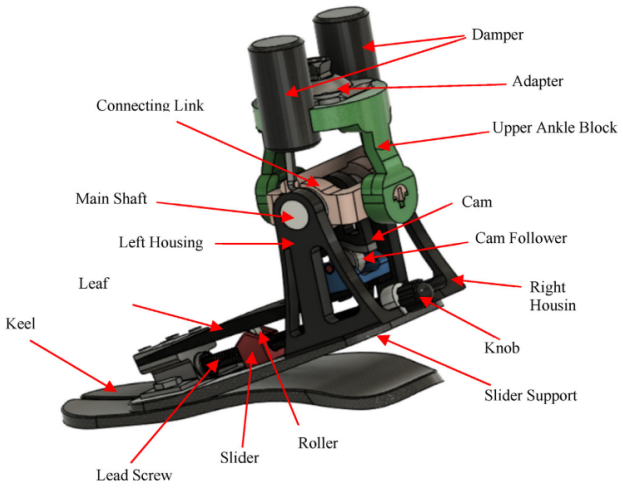


Figure 1.20: CAD model of the ankle-foot prosthesis by V. B.s. and al. [28]

In 2016, Pham et al. [29] developed a passive ankle-foot prosthesis for amputee rehabilitation, where inversion-eversion was damped via a flexure hinge. A schematic is shown in Figure 1.21. This prosthesis remains in prototype form.

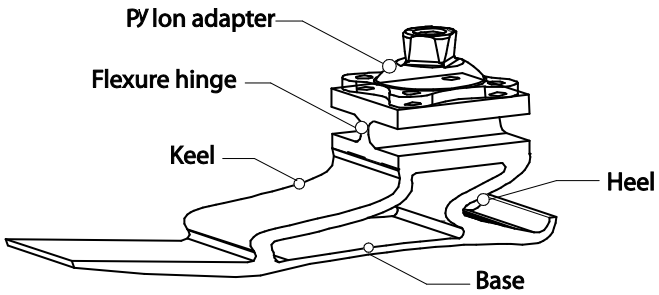


Figure 1.21: Schematic of the ankle-foot prosthesis by Pham et al. [29]

## 1.4 Overview

The state of the art indicates that frontal plane motion in hip prostheses is rarely implemented and never in a passive way. Even for ankle prosthesis, only a few works exists on passive frontal movement. These observations motivate the study to examine a passive mechanism and implement it on an existing prosthesis.

This work covers the full process, from estimating hip stiffness in the frontal plane to assembling a 3D-printed prototype. The prototype's testing protocol is outlined, and future perspectives are discussed in the final chapter.

# Chapter 2

# Frontal plane hip stiffness during walking gait

To design a passive degree of freedom for the prosthesis, hip motion in the frontal plane must first be modeled linearly, as the design will use commercially available linear stiffness springs. This chapter focuses on determining the most suitable linear stiffness of the hip in the frontal plane during walking.

In biomechanical modeling, quasi-stiffness and stiffness are distinct concepts when considering powered joints. However, for passive joints, these concepts are equivalent [30]. Since the focus here is solely on passive joints, only the term stiffness will be used.

## 2.1 Methodology of the study

Axial stiffness describes the resistance of a body to deformation under a force [31]. Since the hip is a spherical joint, its motion is purely rotational. This study therefore considers angular stiffness, defined as the resistance of a body to rotation when subjected to a moment.

To estimate the optimal linear angular stiffness of the hip, the approach involves:

1. Collecting angle and moment data during walking gait,
2. Processing the data,
3. Fitting the data with a linear approximation.

The slope of the moment–angle linear approximation corresponds to the estimated linear stiffness in the frontal plane.

## 2.2 Data processing

Six studies [11, 14, 32–35] were identified via Google Scholar. They report hip frontal plane angles and moments during walking in healthy individuals. These are referred to as "Source 1" through "Source 6". Sources 4 and 5 provide data only for the stance phase.

The data, initially presented as graphs, were digitized using [36]. Figure 2.1 shows the collected data, where positive moments indicate abduction and positive angles indicate adduction.

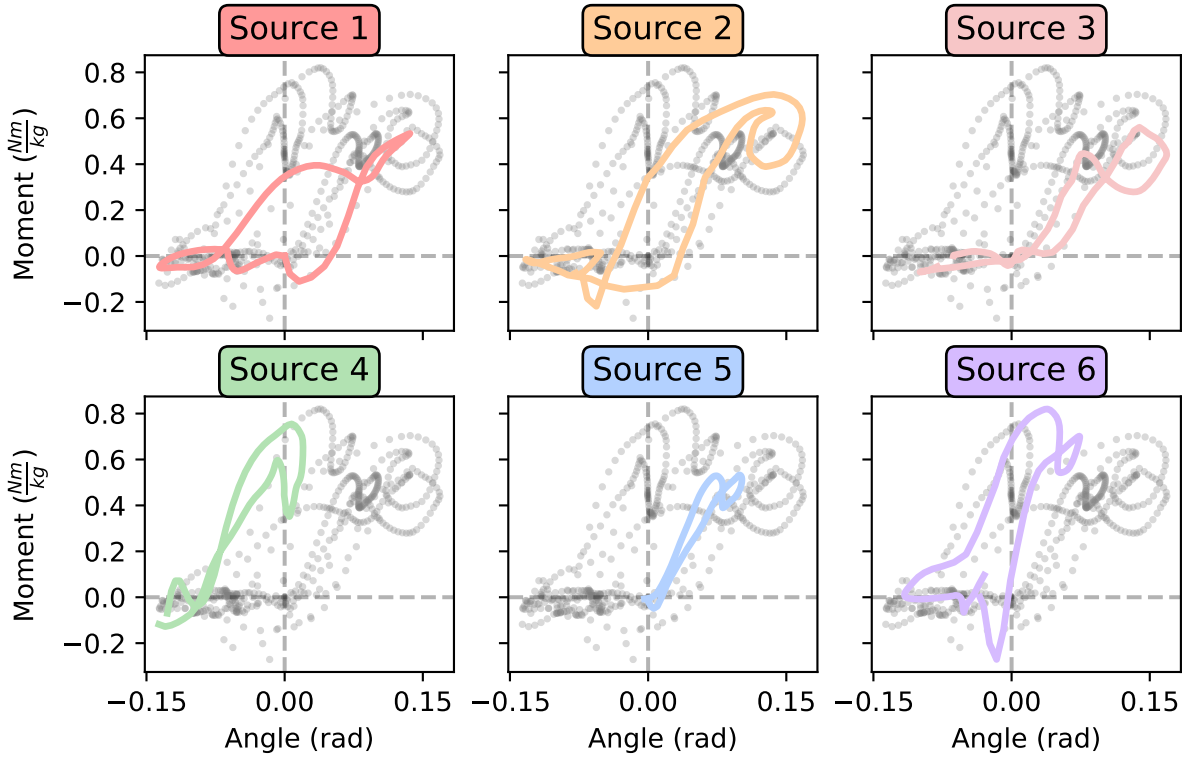


Figure 2.1: Hip moments as a function of frontal plane angles during walking, from six different sources. Colored line : concerned source data; grey points : other sources data.

## 2.3 Linear regression

The goal is to fit the data with a linear regression model. Model performance is assessed with the Root Mean Squared Error (RMSE):

$$RMSE = \sqrt{\frac{1}{n}\sum_{i=1}^{n}(y_i - \hat{y}_i)^2}$$

where $y_i$ is the measured moment for angle $\theta_i$ and $\hat{y}_i$ is the predicted value from the regression.

To account for differences in magnitude between abduction and adduction moments, RMSE is normalized by the maximum moment value extracted from the data for each movement:

$$NRMSE_{Abd} = \frac{RMSE_{Abd}}{0.820}, \quad NRMSE_{Add} = \frac{RMSE_{Add}}{0.271}$$

The maximum moment for abduction is 0.820 $\frac{\mathrm{N\,m}}{\mathrm{kg}}$ and for adduction 0.271 $\frac{\mathrm{N\,m}}{\mathrm{kg}}$. The mean of both $NRMSE$ values is used to evaluate the global fit.

### 2.3.1 Single linear regression (one spring)

A first approach computes a linear regression for each source, then averages the slopes and intercepts. Figure 2.2 shows the result. The errors are $NRMSE_{Abd} = 27.30$ % and $NRMSE_{Add} = 52.14$ %.

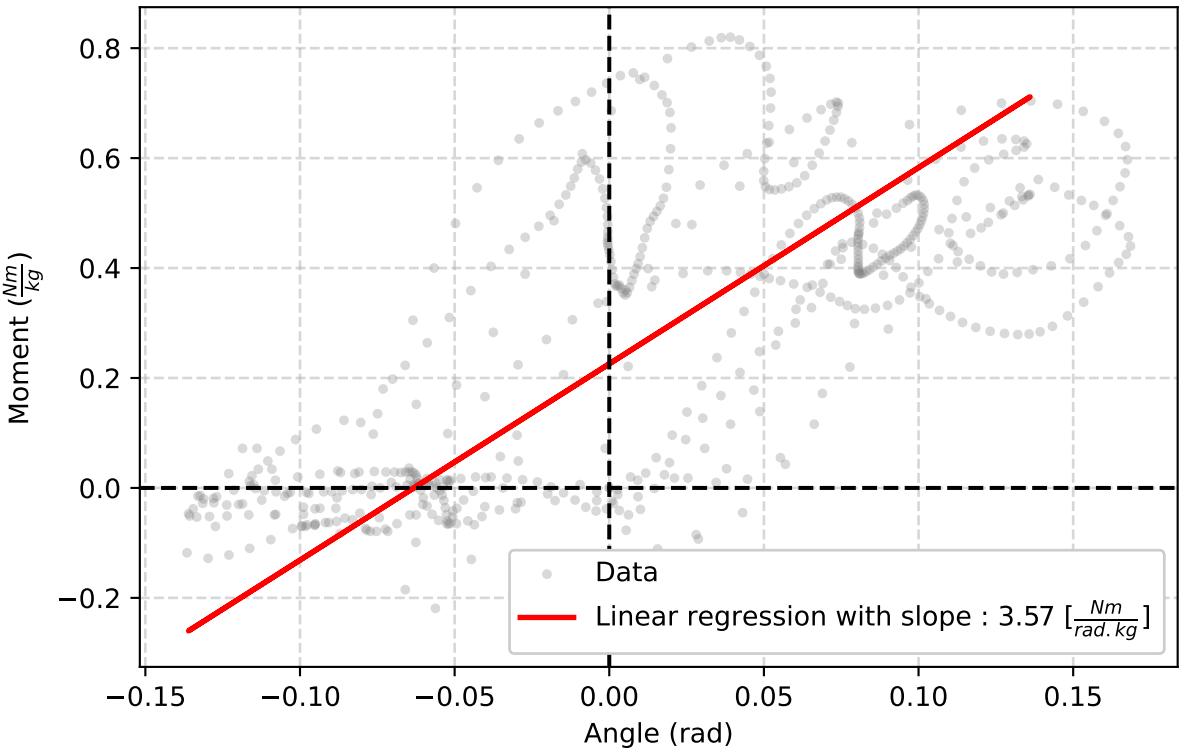


Figure 2.2: Mean of the linear regressions from the six sources. Grey points : data from the 6 sources; red line : linear regression

### 2.3.2 Two linear regressions (two springs)

In order to improve the fit, the data are split into two regions with separate slopes, meeting at a single point $C_x$ on the moment–angle graph. For stability, the meeting point is chosen at zero moment.

The model parameters are:

- $C_x$: meeting point between both lines
- $a_1$: slope for negative moments (positive adduction moment)
- $a_2$: slope for positive moments (positive abduction moment)

Parameters are obtained by minimizing the mean squared error (MSE) for each source (Figure 2.3). Sources 4, 5, and 6 provide too few adduction data points to estimate $a_1$, so these are excluded from the final average for $a_1$ but well keep for the average of $a_2$.

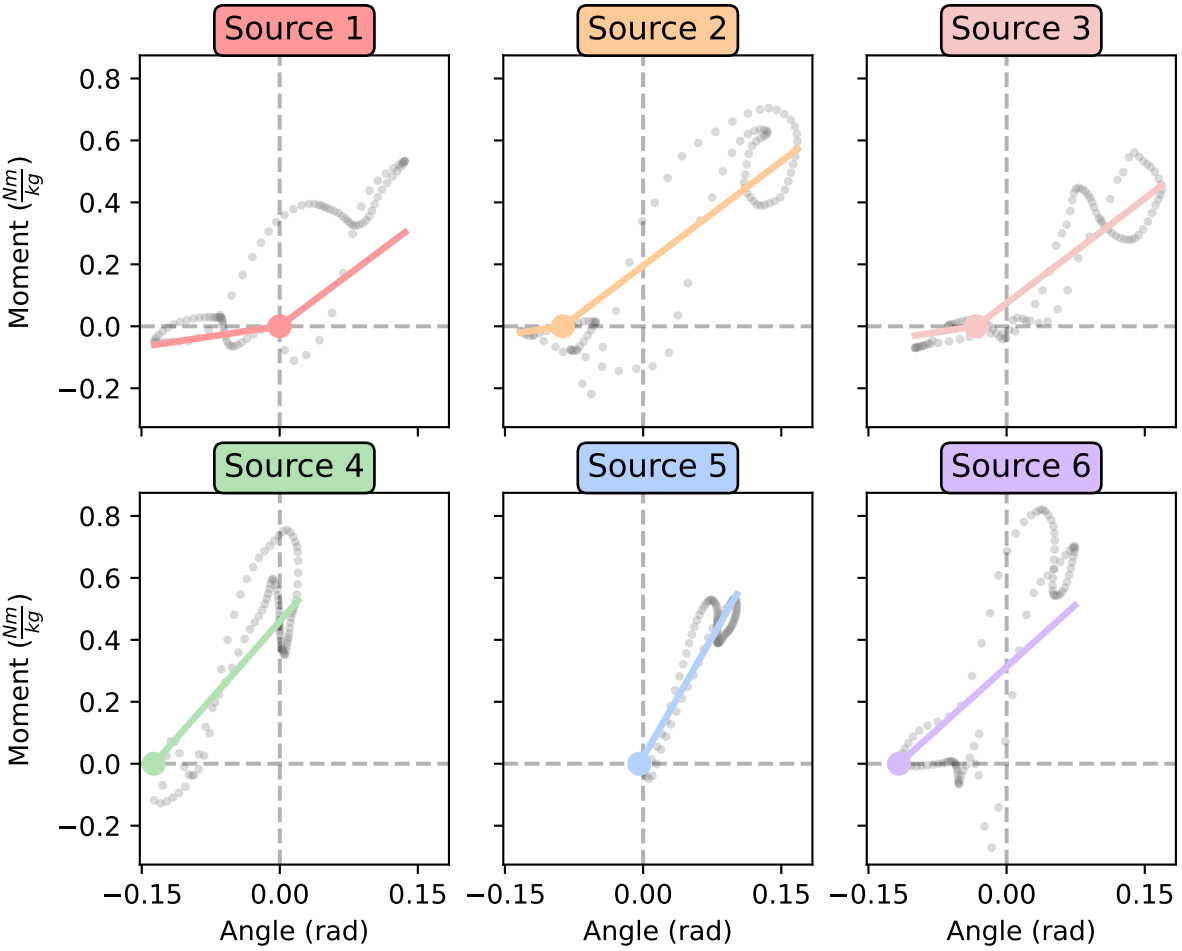


Figure 2.3: Two linear regressions per source, with meeting points. Colored line : regression for the concerned source; grey points : data from the concerned source.

Slope comparisons (Figure 2.4) and meeting point comparisons (Figure 2.5) show no significant outliers.

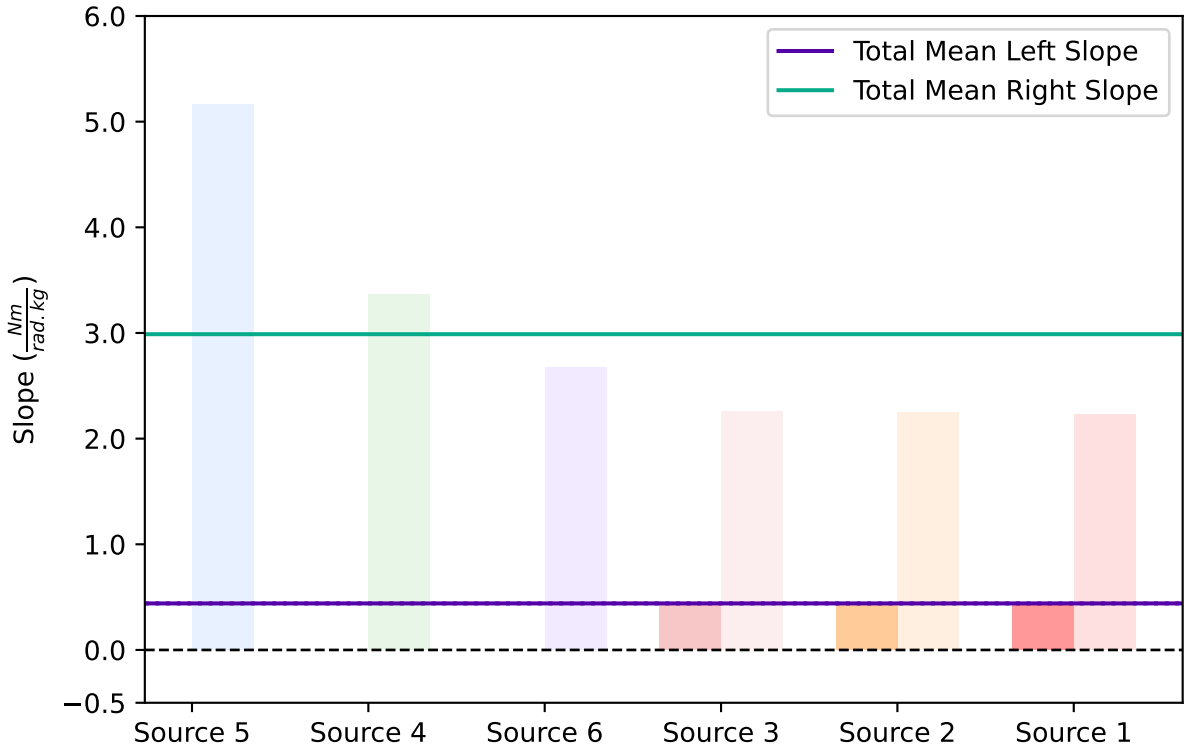


Figure 2.4: Slopes for each source. Bold bars : positive adduction moments region ($a_1$); transparent bars : positive abduction moments region ($a_2$).

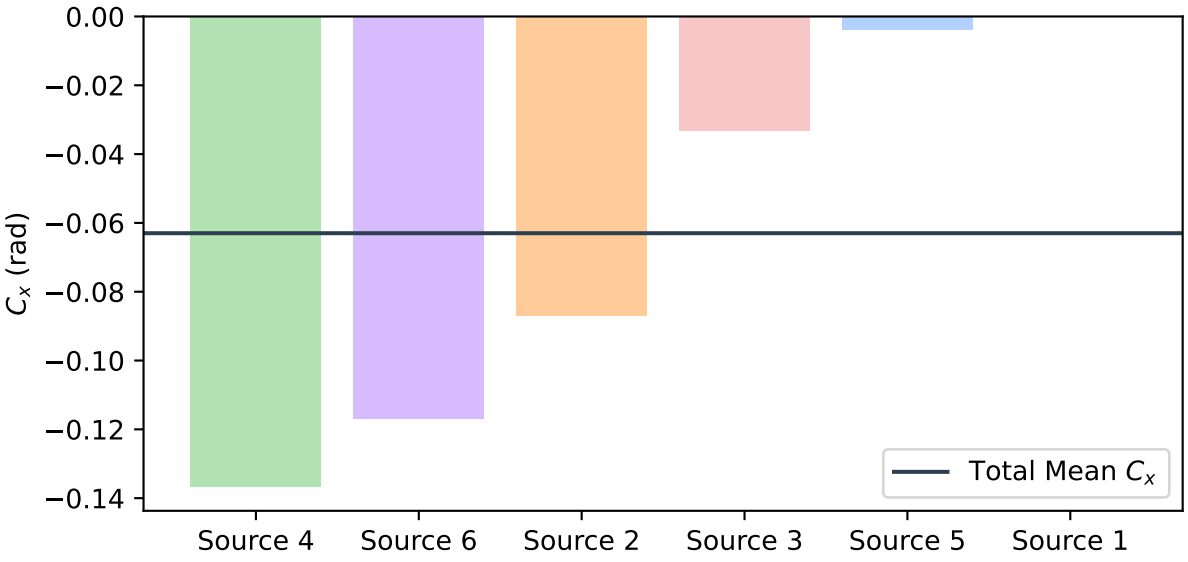


Figure 2.5: Meeting point positions $C_x$ for each source.

Final regression parameters are the mean of valid slopes and $C_x$ values. Figure 2.6 shows the result that give $NRMSE_{Abd} = 25.98$ % and $NRMSE_{Add} = 25.09$ %.

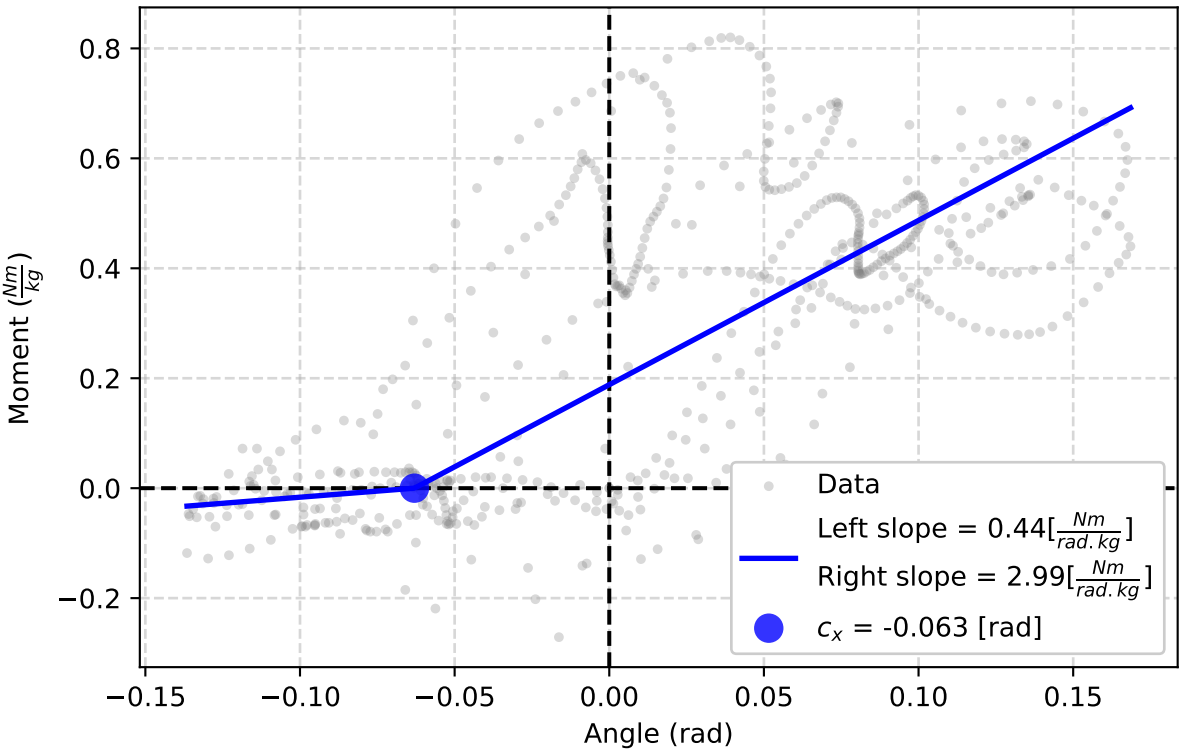


Figure 2.6: Two linear regression for all the data using two lines meeting at $C_x$.

## 2.4 Results

The aim was to approximate the nonlinear stiffness of the hip in the frontal plane during walking with a linear model. When $C_x$ is set at the origin, stiffness is defined separately for adduction (positive angles) and abduction (negative angles). The second method confirms that adduction stiffness is greater than abduction one which seems pretty intuitive because during a walking gait cycle, the adduction movement takes part during the stance phase, where all the body weight is on the leg which ensure the ground contact. But the abduction movement takes part during the swing phase, where the leg is almost completely unloaded.

The mean $NRMSE$ values for both methods are summarized in Table 2.1.

Table 2.1: Normalized errors for the two linear regression models.

| | One linear | Two linear |
|---|---|---|
| $NRMSE_{Abd}$ | 27.30% | 25.98% |
| $NRMSE_{Add}$ | 52.14% | 25.09% |
| $NRMSE_{mean}$ | 39.72% | 25.54% |

The two-slope model (sub-section 2.3.2) performs better overall, mainly by improving accuracy in the negative moment (adduction) region. Nevertheless, the remaining error

reflects that biological hip stiffness during walking is not inherently linear. The choice of a passive degree of freedom justifies the search for linear stiffness values despite this limitation.

# Chapter 3

# Design of the passive degree of freedom

In this chapter, the design of the passive abduction/adduction degree of freedom is presented. This degree of freedom must be implemented on an existing hip prosthesis, originally designed to reproduce hip motion in the sagittal plane (see Figure 1.3). The prosthesis used as the basis of the thesis is the one designed by L. Devillez [26]. For conciseness, the term "prosthesis" will be used throughout this chapter to refer specifically to this device.

The passive degree of freedom is implemented at the base of the prosthesis to ensure that the entire prosthetic leg follows the movement. This choice imposes several design constraints that must be taken into account.

Because the motion requires a linear stiffness (as determined in Chapter 2), springs are chosen as the actuation element. Only springs with linear stiffness are considered.

Once the design constraints are established, the appropriate spring family can be determined, followed by the design process itself. To ensure that the specifications are met (see Appendix A.1), the systematic design methodology described by G. Pahl and W. Beitz [37] is followed. A short summary of this methodology is provided in Appendix A.

Finally, the proposed design is presented first through CAD representations and then by photographs of a 3D-printed prototype at the end of this chapter.

## 3.1 Design constraints

The starting point of the design is the prosthesis made by L. Devillez [26]. This prosthesis is composed of several parts, as shown in Figure 1.19. To implement an additional degree of freedom, the mechanism must be added at the base of the prosthesis to ensure that the entire prosthetic leg moves in the frontal plane. A CAD representation of the initial base is shown in Figure 3.1.

Certain features of the base must remain unchanged. The four holes on the side of the base must remain in their original positions to preserve the trajectory of the four-bar mechanism of the prosthesis. The holes on the upper part of the base are used to attach the prosthesis to the lamination plate in the patient's socket. Their position and size cannot be modified.

The angle of the upper part must remain unchanged to maintain the correct alignment of these attachment points and ensure that the parts of the double parallelogram mechanism are right in place to operate properly.

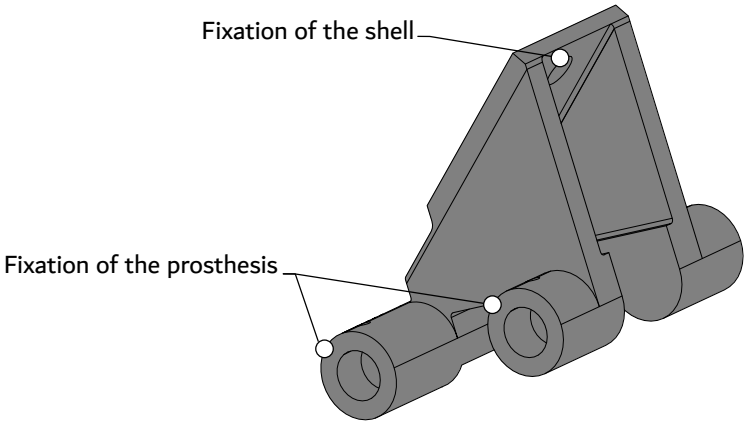


Figure 3.1: 3D view of the original base of the prosthesis.

To implement the new degree of freedom, a shaft-based design was chosen. The morphology of the base must therefore be modified to accommodate this feature. The new design is shown in Figure 3.2. Two mechanical stops are included to limit the maximum angle of the prosthesis in the frontal plane to 7 deg, which was chosen within the range of maximum angles observed in Chapter 2.

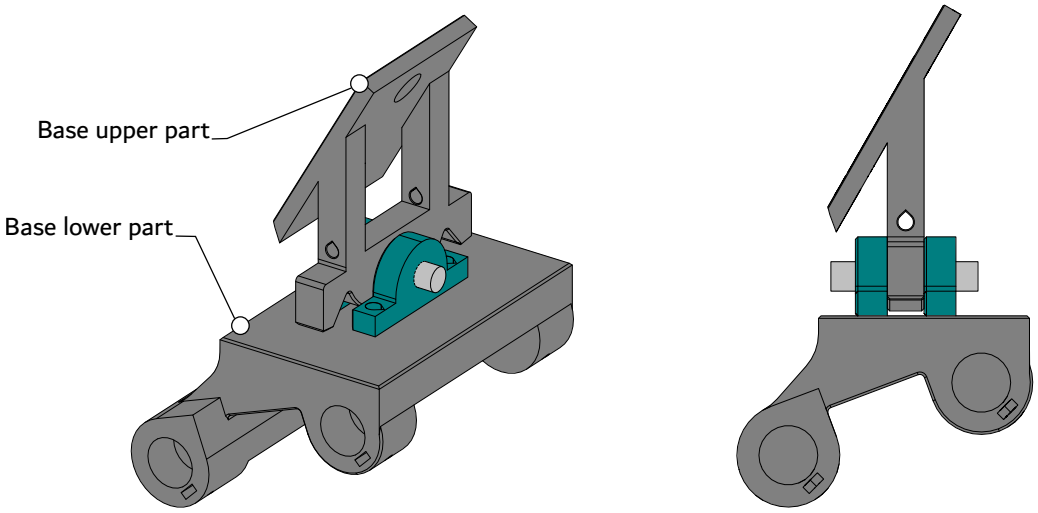


Figure 3.2: Views of the first implementation of a shaft in the base of the prosthesis. Left : 3D view; right : side view (sagittal plane).

## 3.2 Determination of the spring families

To identify the spring family that best fits our problem, it is essential to define the specific requirements. A spring has two major features: stiffness and the potential energy it can store. Both of these characteristics are critical for our application.

It is important to note that, due to the timing of this thesis and a different approach to measuring the regression error compared to Chapter 2, the data used in the following regression are from a previous version of the two linear regression models. This earlier version minimizes the global error rather than minimizing the error separately for each side of the meeting point. As a result, the stiffness and energy values used here differ from the final results presented in the preceding chapter.

### 3.2.1 Determination of the required characteristics

Much of the preliminary work for determining the required spring characteristics was conducted in Chapter 2, where the focus was on estimating an approximate linear stiffness for the hip abduction/adduction movement during walking. The outcome provides a stiffness for each movement. Consequently, the design requires two springs with different stiffness values.

The angle at which the stiffness changes is set at zero degrees for stability purposes. Zero degrees corresponds to the vertical position, where the mechanism must experience zero moment. This design requirement induces a shift in the Moment–Angle graph compared to Figure 2.6.

Keeping this in mind, the problem can be divided into two subproblems: selecting a spring family for the abduction movement and another for the adduction movement.

The energy required by the hip during walking can be obtained by integrating the slopes on the Moment–Angle graph, leading to:

$$E_{req} = \frac{k_\theta(\theta_{max})^2}{2}$$

with $E_{req}$ the required energy in $\frac{\mathrm{J}}{\mathrm{kg}}$, $k_\theta$ the angular stiffness in $\frac{\mathrm{N\,m}}{\mathrm{rad\,kg}}$ and $\theta_{max}$ the maximal angle for a direction (abduction or adduction) in rad.

The maximal angles observed in the six sources analyzed in Chapter 2 are 0.17 rad for the adduction movement and 0.14 rad for the abduction movement. The corresponding required spring characteristics for each movement are summarized in Table 3.1.

Table 3.1: Required features for the springs per each movement

| Required Characteristic | Adduction | Abduction |
|---|---|---|
| Stiffness $\frac{\mathrm{N\,m}}{\mathrm{rad\,kg}}$ | 4.08 | 1.35 |
| Energy $\frac{\mathrm{J}}{\mathrm{kg}}$ | $58.96 \times 10^{-3}$ | $13.23 \times 10^{-3}$ |

The search for a spring must account for body mass because the recovered data are normalized by the mass. According to [38], over a 10-year period, 68 individuals underwent

hemipelvectomy, of which 59% were male and 41% female. This observation drives the study to focus primarily on male body mass.

Furthermore, article [39] reports that the mean body mass for a European adult is 82.2 kg. This data is relevant to our problem because the passengers studied are middle-aged, which corresponds to the typical patient undergoing hemipelvectomy or hip disarticulation [38] (mean age: 43 years).

For this thesis, the selected body mass range is from 70 kg to 120 kg.

### 3.2.2 Comparison between the spring families

To compare different spring types (called spring families in the following), data has to be found about springs. Data were collected from the website of the supplier Inexal, one of the European leaders in the spring market. The choice of Inexal is also driven by the amount of data available on their website concerning springs. The study focuses on these spring families:

- Compression springs
- Traction springs
- Double torsion springs
- Clock springs

The morphology of these different spring families can be seen in Figure 3.3.

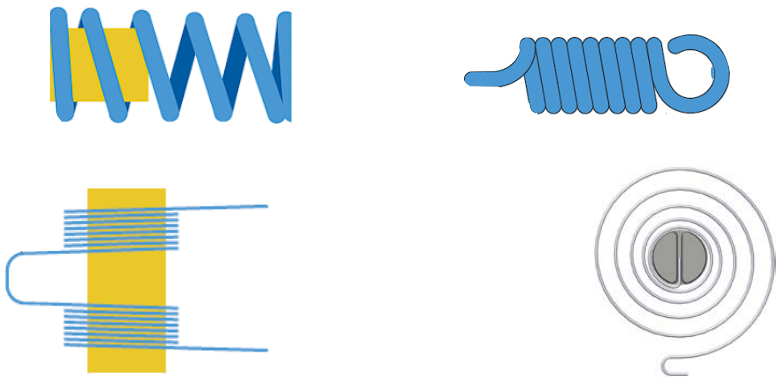

Figure 3.3: Morphology of the four families of springs. Top left : compression; top right : traction; bottom left : double torsion; bottom right : clock.

After collecting all the data from the Inexal catalog, it is important to convert the stiffness into the same units for comparison. Linear springs, such as compression and traction, have axial stiffness in $\frac{\mathrm{N}}{\mathrm{m}}$, while rotational springs, such as double torsion and clock springs, have angular stiffness in $\frac{\mathrm{N\,m}}{\mathrm{rad}}$. Since the required stiffness for the hip movement is in $\frac{\mathrm{N\,m}}{\mathrm{rad}}$, this will be the unit used.

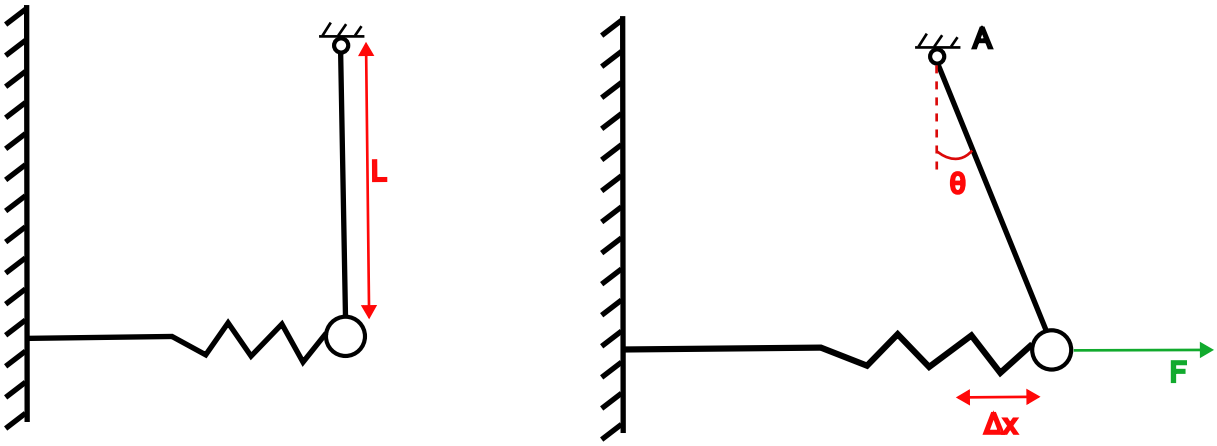


Figure 3.4: Spring-pendulum system to convert axial stiffness into angular stiffness. Left: equilibrium position; right : stretched position

To convert linear stiffness $k$ ($\frac{\mathrm{N}}{\mathrm{m}}$) into angular stiffness $k_\theta$ ($\frac{\mathrm{N\,m}}{\mathrm{rad}}$), a spring-pendulum mechanism is used (Figure 3.4). The length of the pendulum is chosen based on the available length scale of the part to be modified (base of the prosthesis, Figure 3.1). For our application, $L = 50\,\mathrm{mm}$. The moment at point A is given by :

$$M = Lk\Delta x$$

with angular stiffness defined as :

$$k_\theta = \frac{M}{\theta} = \frac{Lk\Delta x}{\arcsin\left(\frac{\Delta x}{L}\right)}.$$

For small angles, $\sin(\frac{\Delta x}{L}) \simeq \frac{\Delta x}{L}$, which gives :

$$k_\theta = L^2 k.$$

The potential energy stored in an axial spring is :

$$E = \frac{k(\Delta x_{\max})^2}{2}.$$

Considering angular stiffness converted or obtained from the catalog of the supplier Inexal, and the energy calculated, springs can be plotted on a stiffness-energy graph. An example of compression springs for the abduction movement is shown in Figure 3.5.

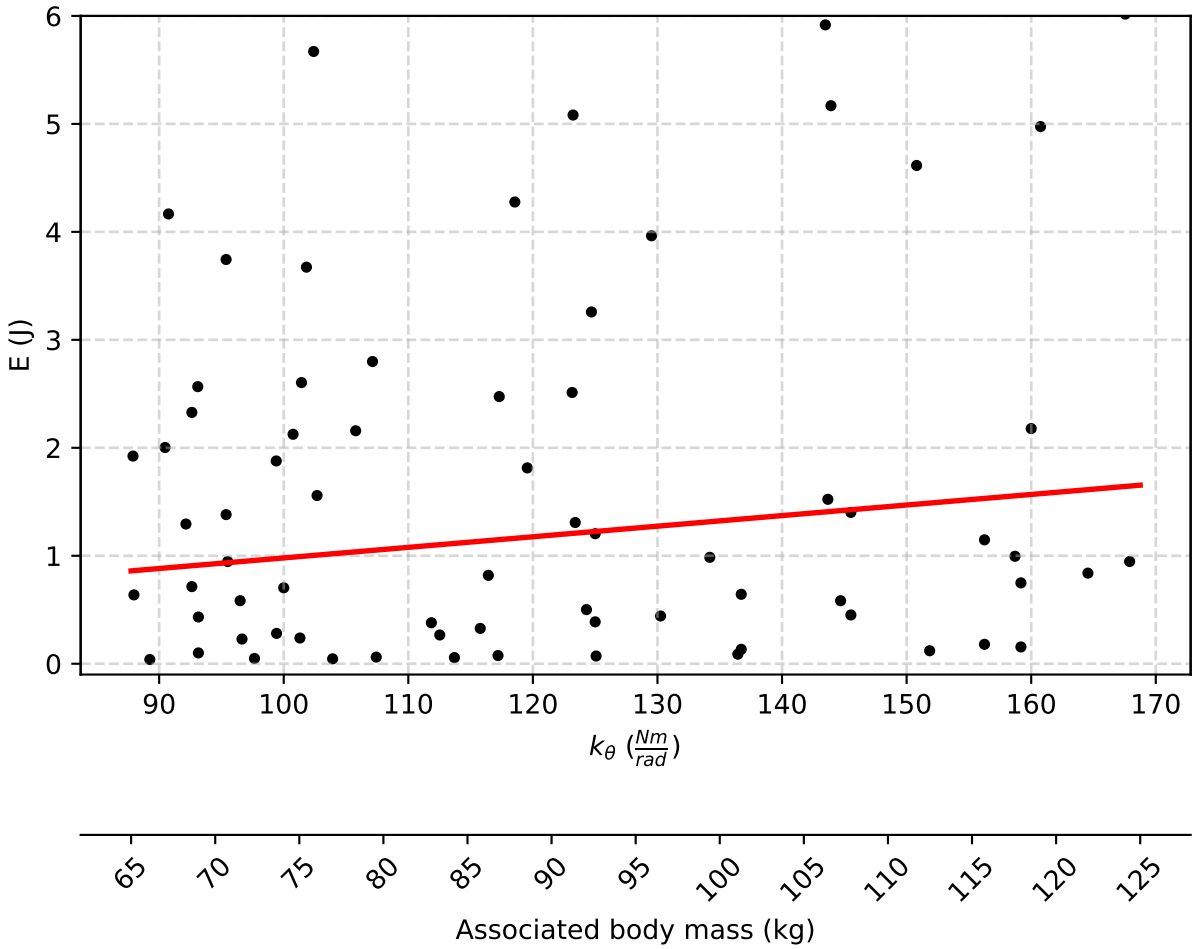


Figure 3.5: Stiffness-energy graph for compression springs (abduction movement). Black points : Inexal springs; red line : theoretical energy needed for the hip for a given body mass.

Springs below the theoretical energy line cannot store enough energy for the application. A maximal energy value is used to filter out the largest springs (Appendix B). To characterize the distance of stiffness between springs, $\Delta k_{\max}$ is defined as the maximum stiffness interval between two springs (Figure 3.6). A smaller $\Delta k_{\max}$ indicates springs are closer horizontally, and the number of springs in the interval can be inferred.

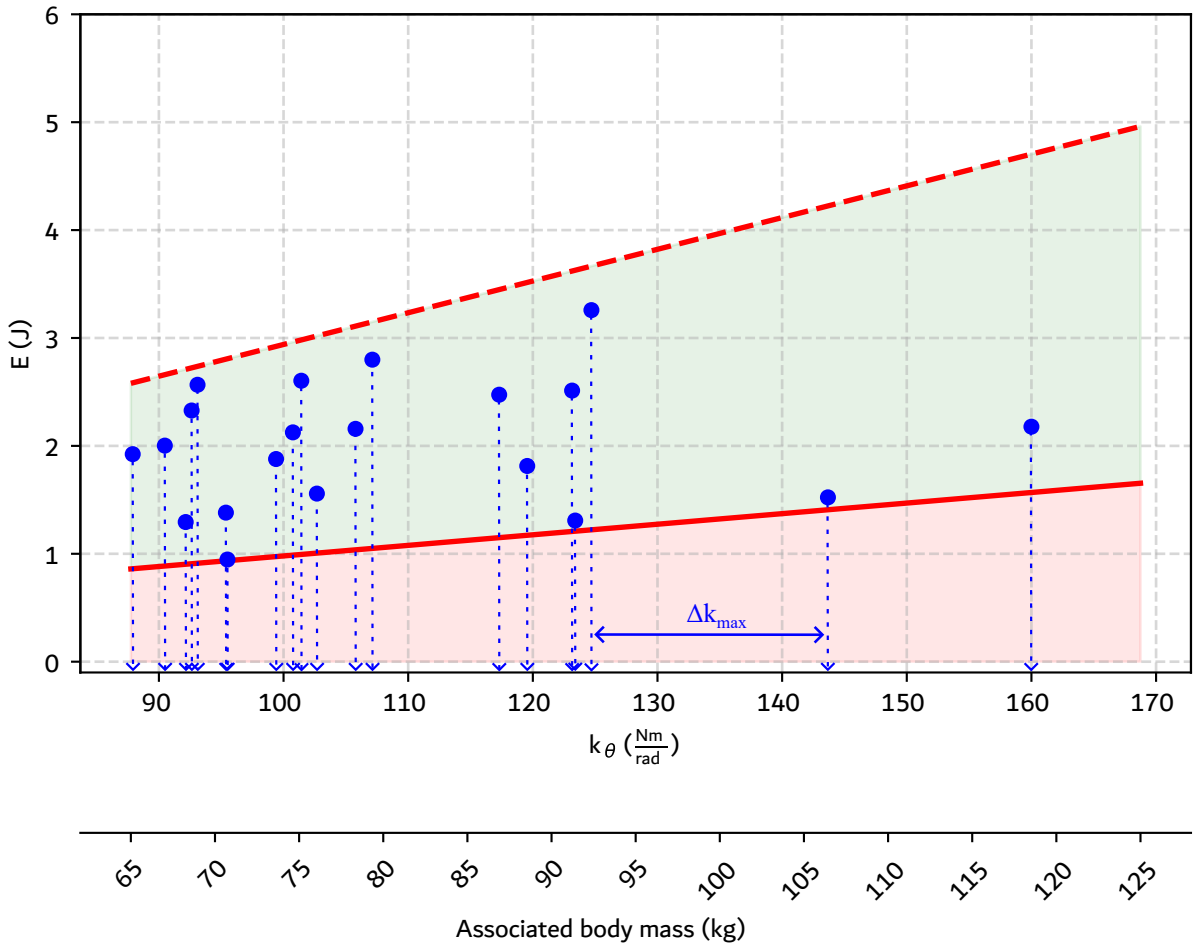


Figure 3.6: Definition of $\Delta k_{\max}$ in the valid interval for compression springs (abduction movement). Solid red line : theoretical energy needed for the hip for a given body mass; Dashed red line : upper limit of energy; blue points : set of valid springs from Inexal catalog.

Using the Inexal data, each spring can be associated with its largest length scale $L_m$. By considering the four spring families and two additional families (two identical compression springs in parallel and two identical traction springs in parallel), we obtain the data shown in Tables 3.2 and 3.3.

Table 3.2: Comparison of mean $\Delta k_{\max}$ and $L_m$ for each spring family in the valid energy interval (adduction movement).

| Criteria | Compression | Traction | Double torsion | Clock | Parallel compression | Parallel traction |
|---|---|---|---|---|---|---|
| Mean $\Delta k_{\max}$ ($\frac{\mathrm{N\,m}}{\mathrm{rad}}$) | 104.7 | NA | 97.79 | 157.73 | 62.23 | 39.92 |
| Mean $L_m$ (mm) | 74.45 | NA | 43.91 | 68.89 | 77.9 | 117.09 |

Table 3.3: Comparison of mean $\Delta k_{\max}$ and $L_m$ for each spring family in the valid energy interval (abduction movement).

| Criteria | Compression | Traction | Double torsion | Clock | Parallel compression | Parallel traction |
|---|---|---|---|---|---|---|
| Mean $\Delta k_{\max}$ ($\frac{\mathrm{N\,m}}{\mathrm{rad}}$) | 21.28 | 63.67 | 30.98 | 98.00 | 15.92 | 15.23 |
| Mean $L_m$ (mm) | 69.77 | 51.83 | 27.56 | 39.2 | 65.55 | 94.02 |

Based on evaluation matrices (Tables 3.4 and 3.5), the double torsion spring family is chosen for both movements for further design steps.

Table 3.4: Evaluation matrix to evaluate the springs for the adduction movement.

| | - - | - | 0 | + | ++ |
|---|---|---|---|---|---|
| Mean $\Delta k_{\max}$ ($\frac{\mathrm{N\,m}}{\mathrm{rad}}$) | $> 200$ | 100–200 | 100 | 40–100 | $< 40$ |
| Mean $L_m$ weight = 2 | $> 100$ | 70–100 | 70 | 50–70 | $< 50$ |

Table 3.5: Evaluation matrix to evaluate the springs for the abduction movement.

| | - - | - | 0 | + | ++ |
|---|---|---|---|---|---|
| Mean $\Delta k_{\max}$ $(\frac{\mathrm{N\,m}}{\mathrm{rad}})$ | $> 70$ | 30–70 | 30 | 20–30 | $< 20$ |
| Mean $L_m$ weight = 2 | $> 70$ | 50–70 | 50 | 30–50 | $< 30$ |

### 3.2.3 Selection of the springs

The double torsion springs available within the selected stiffness intervals are shown in Figure 3.7 for each movement.

Considering the approximations made in the previous analysis, it is not necessary to have a specific pair of springs for each body mass. The goal here is to propose three different sizes, each corresponding to a different equivalent body mass, based on the springs available from Inexal. The commercial reference of the springs and their associated equivalent body masses are presented in Table 3.6. The chosen springs are highlighted in Figure 3.7.

Table 3.6: Three pairs of springs corresponding to three different stiffness values. Sizes are provided for direct reference to the theoretical body mass associated. The commercial reference of the springs from the Inexal catalog are given.

| Size | Ref. Add. | Eq. body mass Add. | Ref. Abd. | Eq. body mass Abd. |
|---|---|---|---|---|
| S | DWT200530 | 76.0 | DWT200390 | 76.4 |
| M | DWT200520 | 85.5 | DWT200380 | 86.4 |
| L | DWT200640 | 107.1 | DWT200490 | 107.9 |

For the purposes of this master thesis, the size S springs will be considered for the subsequent design steps.

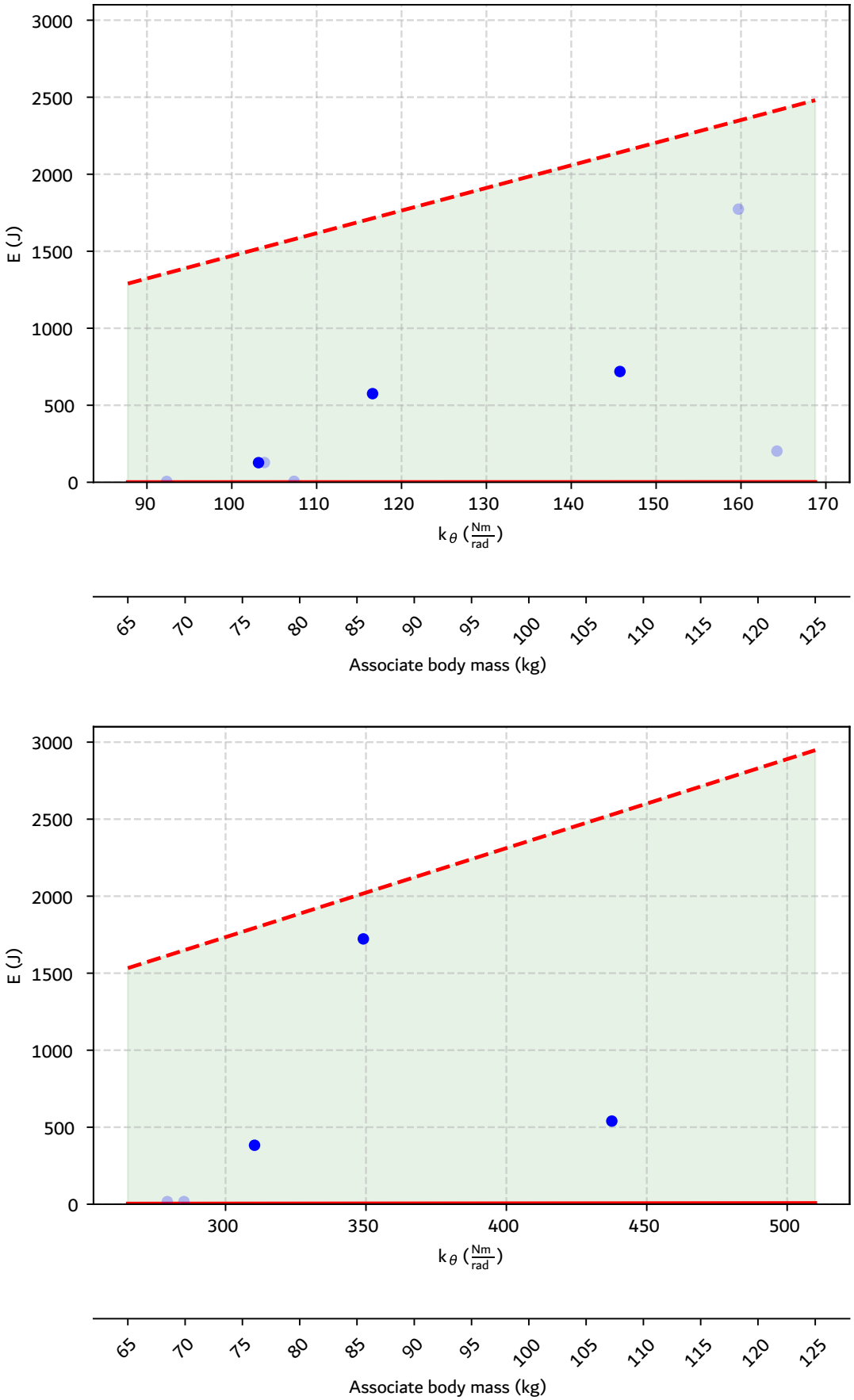


Figure 3.7: Double torsion springs available for each movement, represented in the energy-stiffness graph. Top : Abduction movement; Bottom : Adduction movement.

## 3.3 Dimensioning of the shaft

This section is dedicated to the dimensioning of the shaft. The methodology followed is the one explained by R.C. Juvinall in [40]. As explained earlier, Figure 3.2 shows the morphology proposed to achieve the new degree of freedom on the existing prosthesis.

### 3.3.1 Hypotheses

The following hypotheses are used to dimension this shaft:

- The worst-case scenario corresponds to the heaviest person, with a body mass of 120 kg.
- To account for the impact on the ground during walking, a factor of 2 is applied to the mass [41] and expressed as the weight of the human body perceived during a foot-ground shock :

$$w_h = 2354.4\,\text{N}$$

- The shaft will be purchased from the supplier Misumi. The proposed material chosen is steel EN 1.1191 with the following mechanical properties :
  - Yield stress: $\sigma_y = 413.7\,\text{MPa}$
  - Ultimate stress: $\sigma_u = 620.5\,\text{MPa}$
- For fatigue dimensioning, an amputee walks approximately 3047 steps per day [42]. The shaft is designed for 10 years of use, corresponding to roughly $10^6$ cycles.
- The mass of a prosthetic leg in the worst case is 11.9 kg [26].

### 3.3.2 Static dimensioning during stance phase

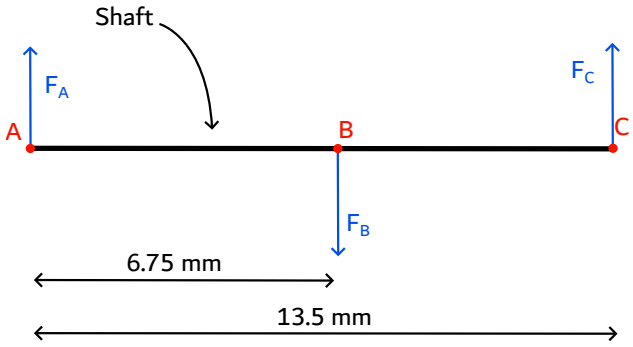


Figure 3.8: Schematic representation of the forces acting on the shaft in the sagittal plane during stance phase with the components shown in Figure 3.2.

During the stance phase, the leg is in contact with the ground, and the shaft undergoes bending. A sketch of the situation is shown in Figure 3.8.

By considering a safety factor of 2 on the body mass, the maximal weight considered is :

$$F_B = 4708.8\,\text{N}$$

Force analysis gives:

$$\sum M_A = 0 \Longrightarrow -6.75F_B + 13.5F_C = 0 \Longrightarrow F_C = \frac{F_B}{2}$$

$$\sum F_v = 0 \Longrightarrow F_A = F_C = \frac{F_B}{2} = 2354.4\,\mathrm{N}$$

The resulting loading diagrams are shown in Figure 3.9.

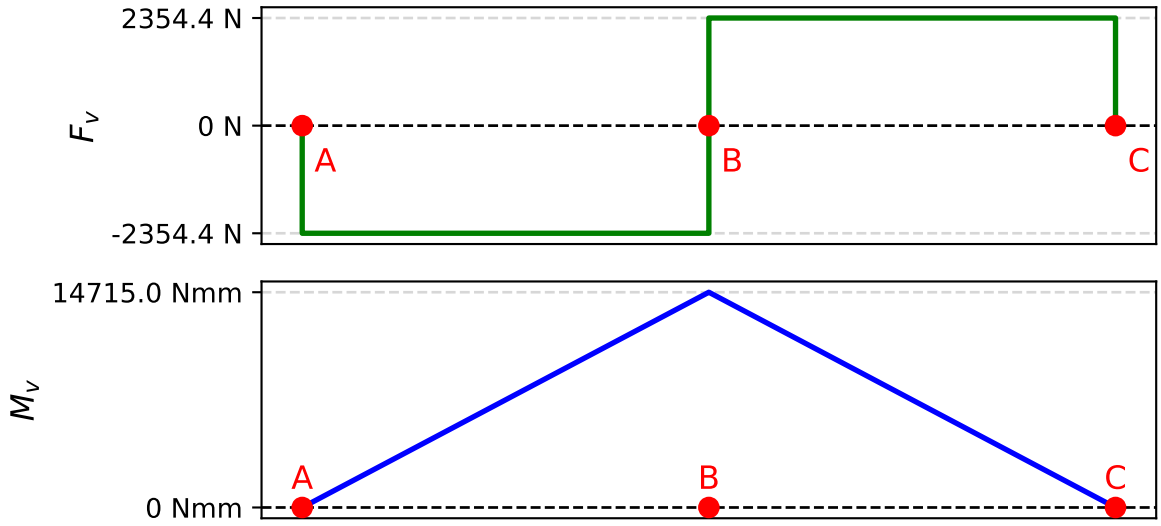


Figure 3.9: Loading diagrams during bending of the shaft (stance phase) in the sagittal plane. A schematic of the loads is given on Figure 3.8. Top : shear force diagram; bottom : bending moment diagram

The maximum moment is :

$$M_{max} = 14.7\,\mathrm{N\,m}$$

Assume that the shaft has to stay in the elastic region and the stress concentration factor $K_t = 1$ (no fillet):

$$\sigma_{max} = \frac{32K_tM_{max}}{\pi d^3} < \sigma_y$$

which leads to:

$$d \geq 7.13\,\mathrm{mm}$$

### 3.3.3 Fatigue dimensioning

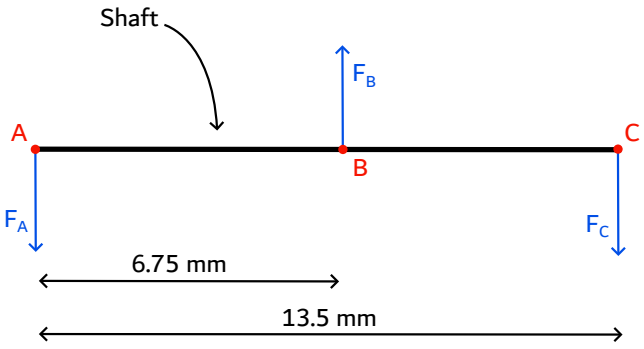


Figure 3.10: Schematic representation of forces acting on the shaft in the sagittal plane during swing phase.

Fatigue arises from gait cycles. During the swing phase, the shaft bends in the opposite direction compared to the stance phase. Figure 3.10 illustrates the forces during the swing phase. Considering the prosthetic leg's weight and a safety factor of 2:

$$w_l = 233.5\,\mathrm{N}$$

Force analysis gives :

$$F_A = F_C = \frac{F_B}{2} = 116.739\,\mathrm{N}$$

Loading diagrams are shown in Figure 3.11.

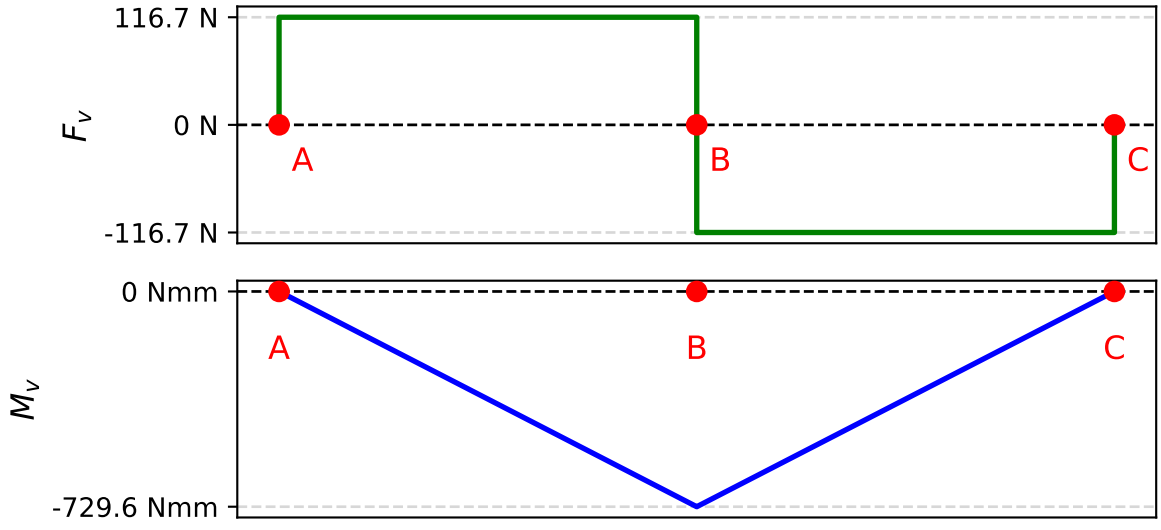


Figure 3.11: Loading diagram during bending of the shaft (swing phase) in the sagittal plane. A schematic of the loads is given on Figure 3.10. Top : shear force diagram; bottom : bending moment diagram

The minimum moment during the cycle is :

$$M_{min} = -0.73\,\mathrm{N\,m}$$

Fatigue constraints :

- $\sigma_{min} = \frac{32M_{min}}{\pi d^3} \implies \sigma_{min} d^3 = -7.44\,\text{Pamm}^3$
- $\sigma_{max} = \frac{32M_{max}}{\pi d^3} \implies \sigma_{max} d^3 = 149.89\,\text{Pamm}^3$
- $\sigma_m d^3 = \frac{\sigma_{max}+\sigma_{min}}{2} d^3 = 71.23\,\text{Pamm}^3$
- $\sigma_a d^3 = \frac{\sigma_{max}-\sigma_{min}}{2} d^3 = 78.67\,\text{Pamm}^3$

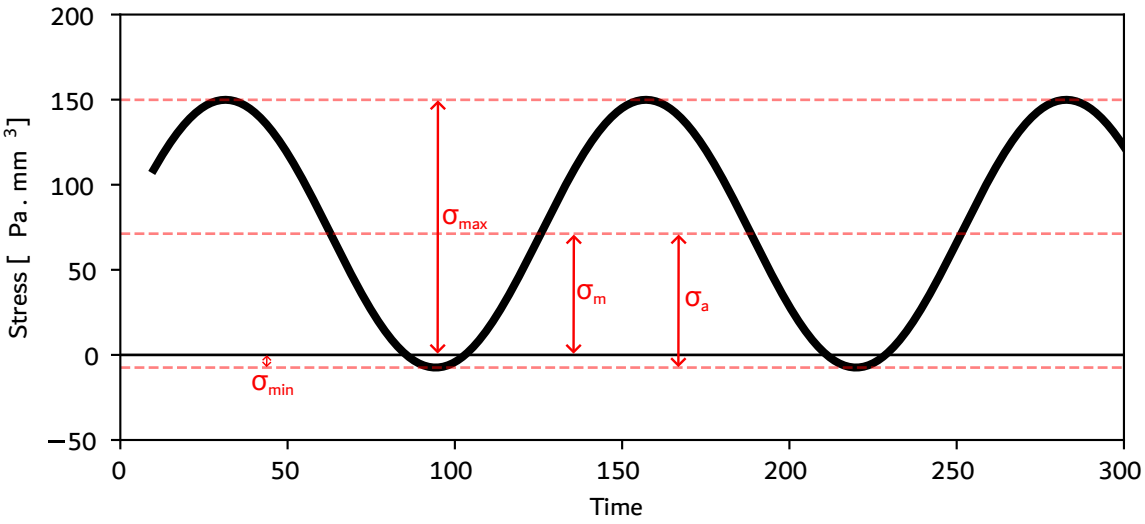


Figure 3.12: Fluctuating stress in the shaft in the sagittal plane during gait cycles.

The next step is to calculate the equivalent alternating bending stress and the equivalent mean bending stress. Since the shaft can rotate freely about its own axis, there is no torsional stress; it is subjected to pure bending. Any torsional effect due to bending is already accounted for in the Von Mises stress $\sigma$. Therefore, the equivalent alternating bending stress equals the maximum alternating stress, and the equivalent mean bending stress equals the maximum mean bending stress :

$$\sigma_{ea,max} = \sigma_{a,max}, \quad \sigma_{em,max} = \sigma_{m,max}$$

As mentioned earlier, the stress concentration factor $K_t = 1$. This implies that the fatigue stress concentration factor $K_f = 1$, which means $\sigma_{a,max} = \sigma_a$. Using the same reasoning, $\sigma_{m,max} = \sigma_m$. This gives:

$$\sigma_{ea,max} = \frac{78.67}{d^3}\,\text{Pa}, \quad \sigma_{em,max} = \frac{71.23}{d^3}\,\text{Pa}$$

To calculate the endurance limit $S_n$, several assumptions need to be made:

- Considering the worst-case scenario, the standard fatigue strength $S'_n$ is taken as half of the ultimate strength $\sigma_u$.
- Since the shaft is subjected only to bending, the load factor $C_l$ is set to 1.
- Due to the geometry of the shaft, the size factor $C_g$ is also taken as 1.

- Based on the value of $\sigma_u$ and the surface finish provided by Misumi, the surface factor $C_s$ is 0.78.
- As the shaft operates at ambient temperature, the temperature factor $C_T$ is set to 1.
- The reliability factor is chosen for a 95 % reliability, giving $C_R = 0.868$.

Using these assumptions, the endurance limit for $10^6$ cycles can be calculated as:

$$S_n = S'_n \cdot C_L \cdot C_G \cdot C_S \cdot C_T \cdot C_R = 210.05\,\text{MPa}$$

With all factors combined, the load line can be determined with a slope of:

$$\frac{\sigma_a}{\sigma_m} = 1.10$$

The corresponding curves are shown in Figure 3.13. From this graph, the red point indicates the intersection, occurring at $\sigma_{a,I} = 160.65\,\text{MPa}$. To ensure safe operation during $10^6$ cycles, the shaft must satisfy:

$$\begin{aligned} & \sigma_{ea,max} \leq \sigma_{a,I} \\ \implies & \frac{78.67}{d^3} \leq 160.65 \times 10^6 \\ \implies & d \geq 7.9\,\text{mm} \end{aligned}$$

Since fatigue dimensioning is more restrictive than static dimensioning, the conclusion is that the shaft should have a diameter greater or equal to 7.9 mm.

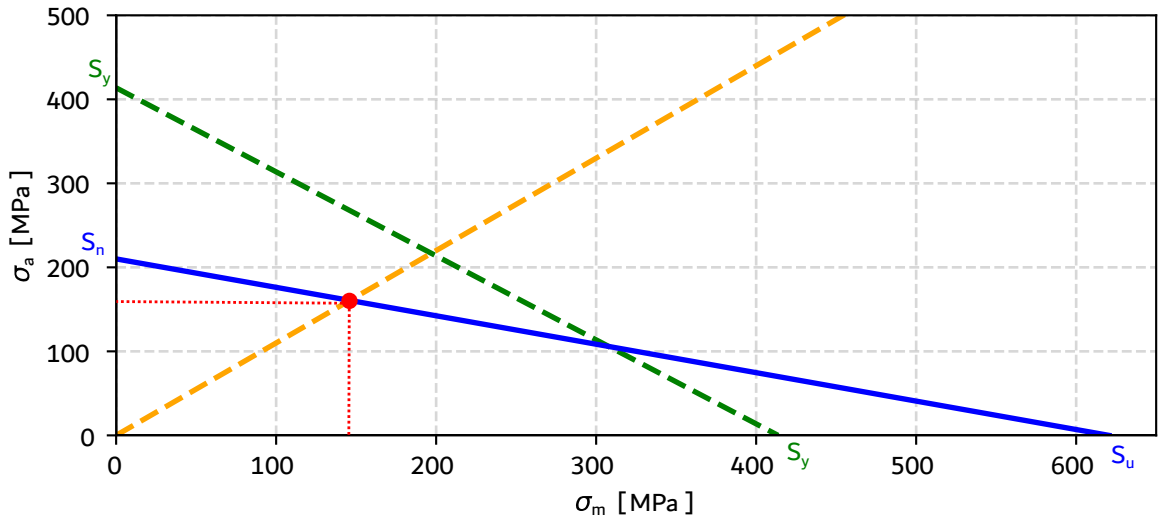


Figure 3.13: $\sigma_m - \sigma_a$ curve (blue line) for $10^6$ cycles. Green dashed line: yield line; orange dashed line: load line.

## 3.4 Detailed design

This section presents a detailed description of the design of the degree of freedom on the modified base of L. Devillez's prosthesis.

### 3.4.1 Shaft assembly

The components of the shaft assembly are shown in Figure 3.14. To clarify how these parts fit together, a sectional view of the assembly is presented in Figure 3.15.

The assembly requires a shaft with a shoulder. Unfortunately, the supplier Misumi does not offer a shaft with this feature and the required dimensions. Therefore, the selected solution is to design a custom shaft adapter secured with a set screw and order a shaft with a D-cut to lock this adapter. These components are illustrated in Figure 3.15. The ordered shaft from Misumi has the reference SSFRHP8-21_5-F25-P5-FC7-G14. It has a diameter of 8 mm in the region where loads are applied, respecting the values calculated in the dimensioning section (section 3.3).

The front and rear fixations are attached to the lower part of the base (see Figure 3.20) and rotate around the shaft. To minimize friction between the adapter and the fixations, as well as between the shaft and the fixations and to guide rotation, two plain bearings are added. The references for these Misumi plain bearings are JZF8-6.

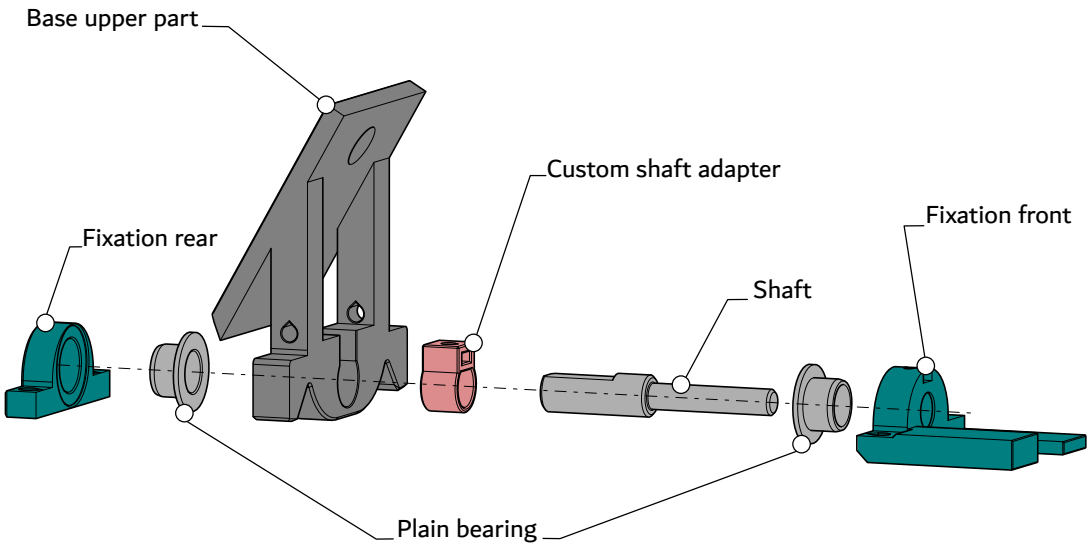


Figure 3.14: Components of the shaft assembly.

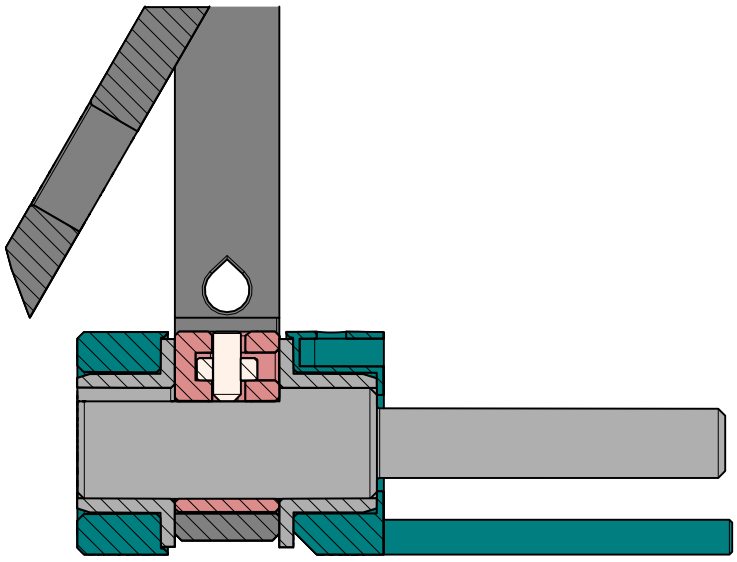

Figure 3.15: Side (sagittal plane) sectional view of the shaft assembly.

### 3.4.2 Spring positioning and degree of freedom actuation

To constrain the springs and ensure they function properly, additional components are added to the shaft assembly, as shown in Figure 3.16. First, the springs need to be guided along the rotation axis of the prosthesis to stay consistent with the calculations presented in Chapter 2. To achieve this, the shaft is extended with a thinner section to guide the springs. This part of the shaft does not carry any load and is solely designed to guide the two springs. Consequently, there is no need to dimension this part; its diameter is chosen based on the smaller inner diameter of the springs.

The second requirement is to maintain the alignment between the springs and the rotation axis. Since the front fixture pushes the springs upward, a "springs blocking" part is added to push them downward and keep them in place. This component also prevents the springs from rotating around the shaft, fully constraining them.

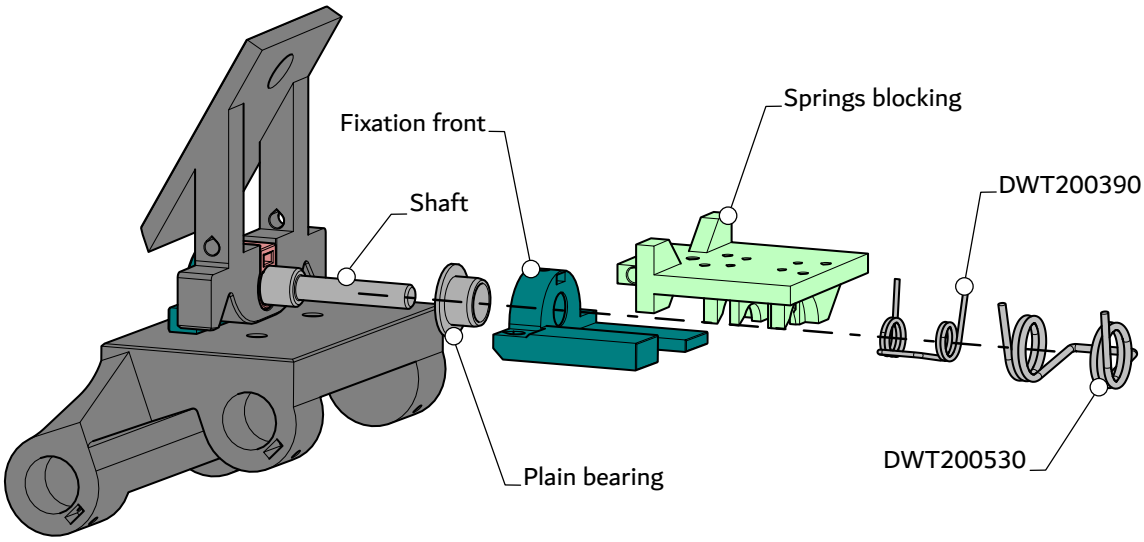


Figure 3.16: Parts used to constrain the springs.

### 3.4.3 Final global design

This subsection presents the final design after implementing the previous modifications, along with additional adjustments for compatibility with 3D printing. The design uses captive nuts instead of internal threads where necessary. Some parts were also modified in shape to ensure printability and functionality. A 3D view of the redesigned base, including the new degree of freedom in the frontal plane, is shown in Figure 3.17.

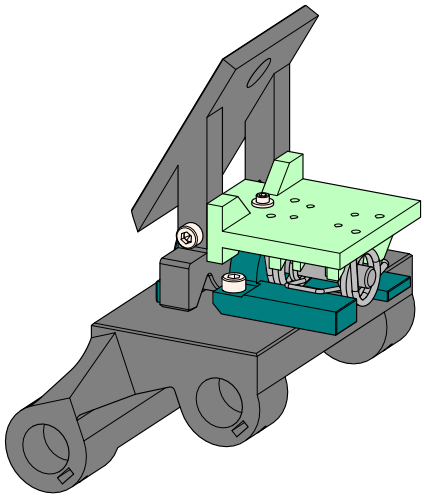

Figure 3.17: 3D view of the redesigned prosthesis base.

Figure 3.18 shows a comparison between the original base and the modified base with the new degree of freedom, highlighting the changes from both front and side views. The Figure 3.18 includes reference dimensions to provide a sense of scale. Figure 3.19 further illustrates this by overlaying the side views of both bases.

Figures 3.20 and 3.21 show the screws used to assemble the shaft assembly and the springs blocking assembly, respectively. The blocking screw visible in Figure 3.22 serves to lock the degree of freedom, as specified in Appendix A.1.

Finally, Figure 3.23 shows the modified base attached to the shell and the prosthesis, and Figure 3.24 illustrates the standing position of the prosthesis along with its two extrema in the frontal plane, demonstrating compatibility between the modified base and the prosthesis.

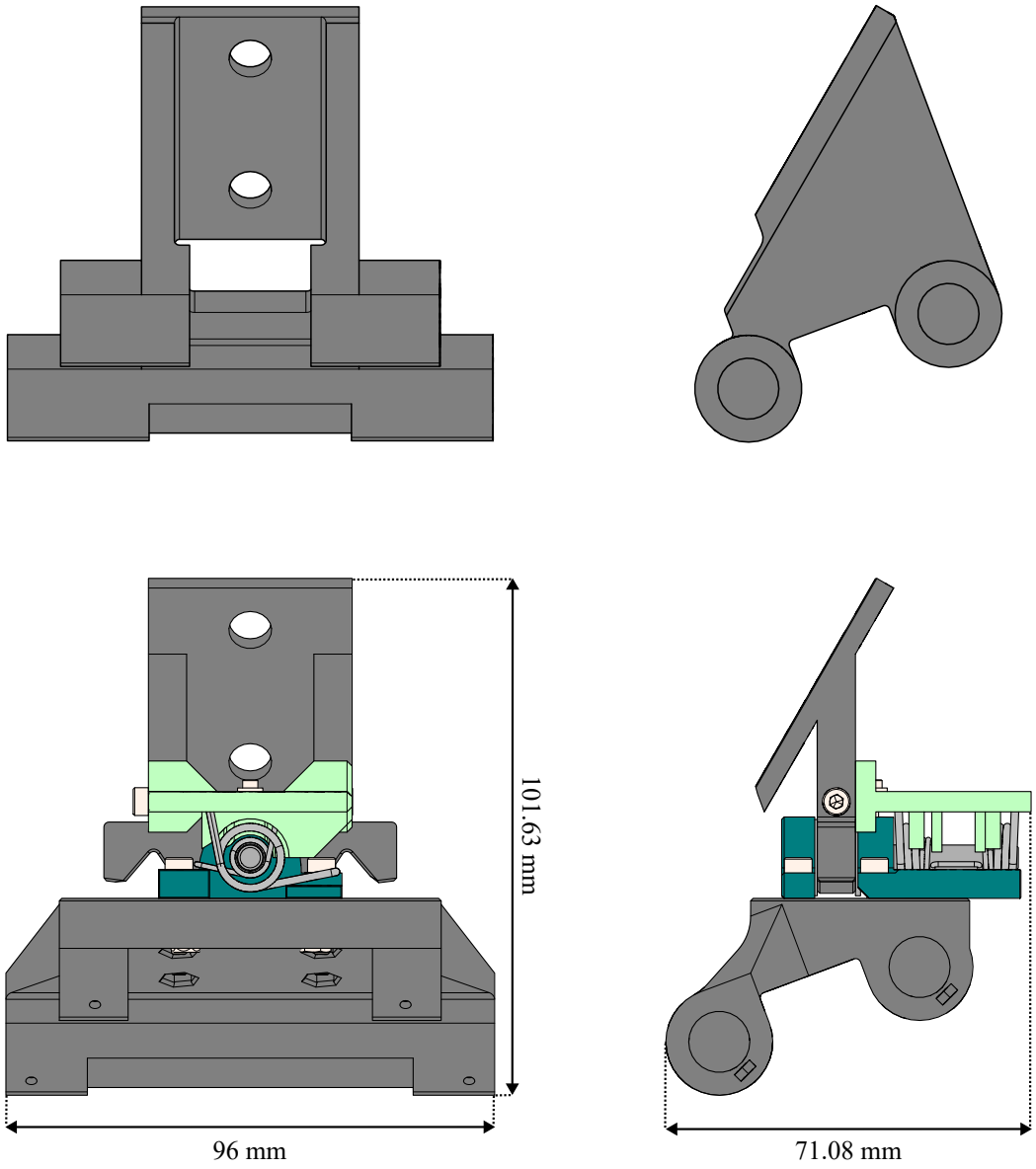


Figure 3.18: Comparison of the original prosthesis base and the modified base with reference dimensions. Top left : Front view (frontal plane) of the original base; top right : side view (sagittal plane) of the original base; bottom left : front view (frontal plane) of the re-designed base; bottom right : side view (sagittal plane) of the re-designed base.

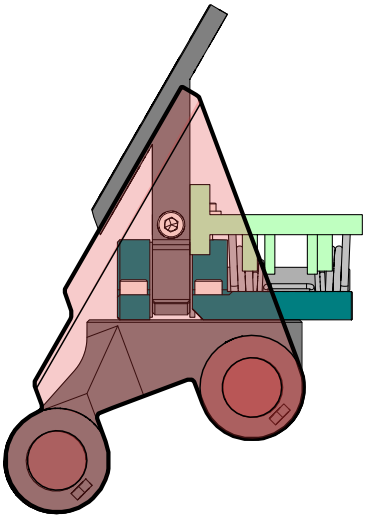

Figure 3.19: Overlay of the side views (sagittal plane) of the original and re-designed base. Red : original base; colored : re-designed base.

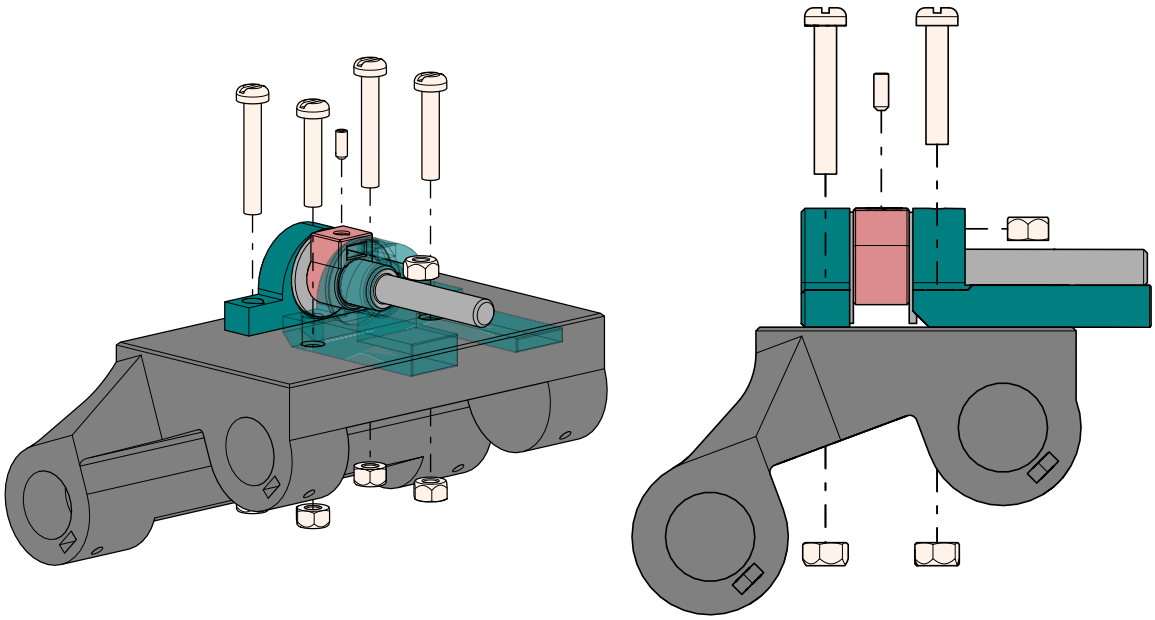

Figure 3.20: Screws securing the shaft assembly to the lower part of the base. The upper part is omitted for clarity. Left : 3D view; right : side view (sagittal plane).

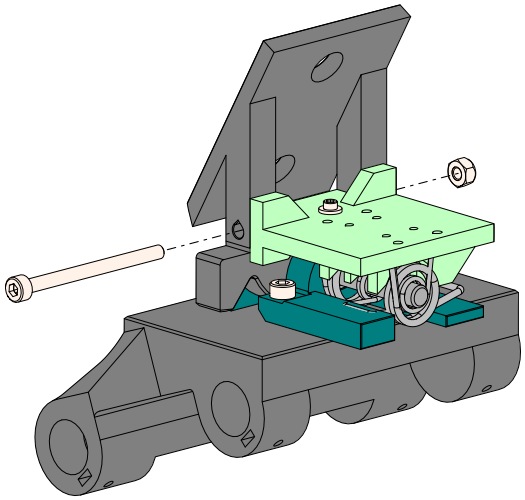

Figure 3.21: 3D view of the re-designed base of the prosthesis with the screw fastening the spring assembly highlighted.

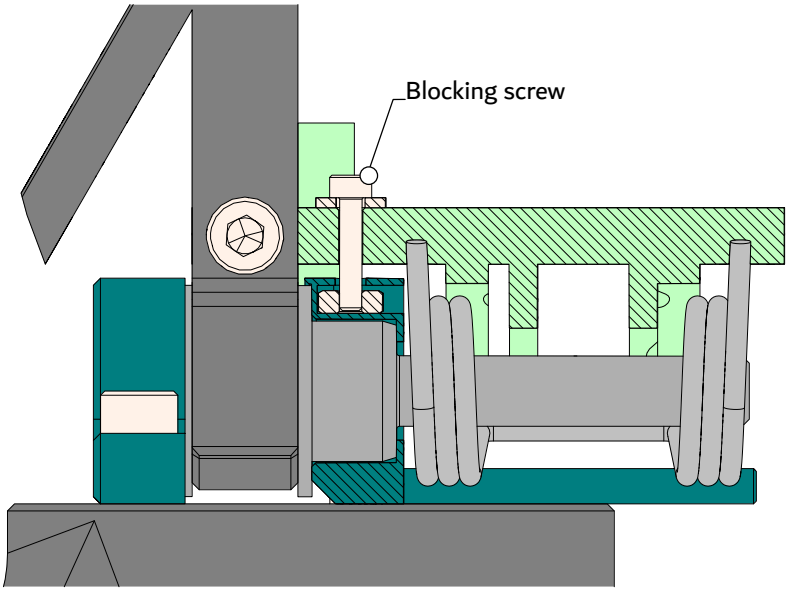


Figure 3.22: Side (sagittal plane) sectional view of the blocking mechanism.

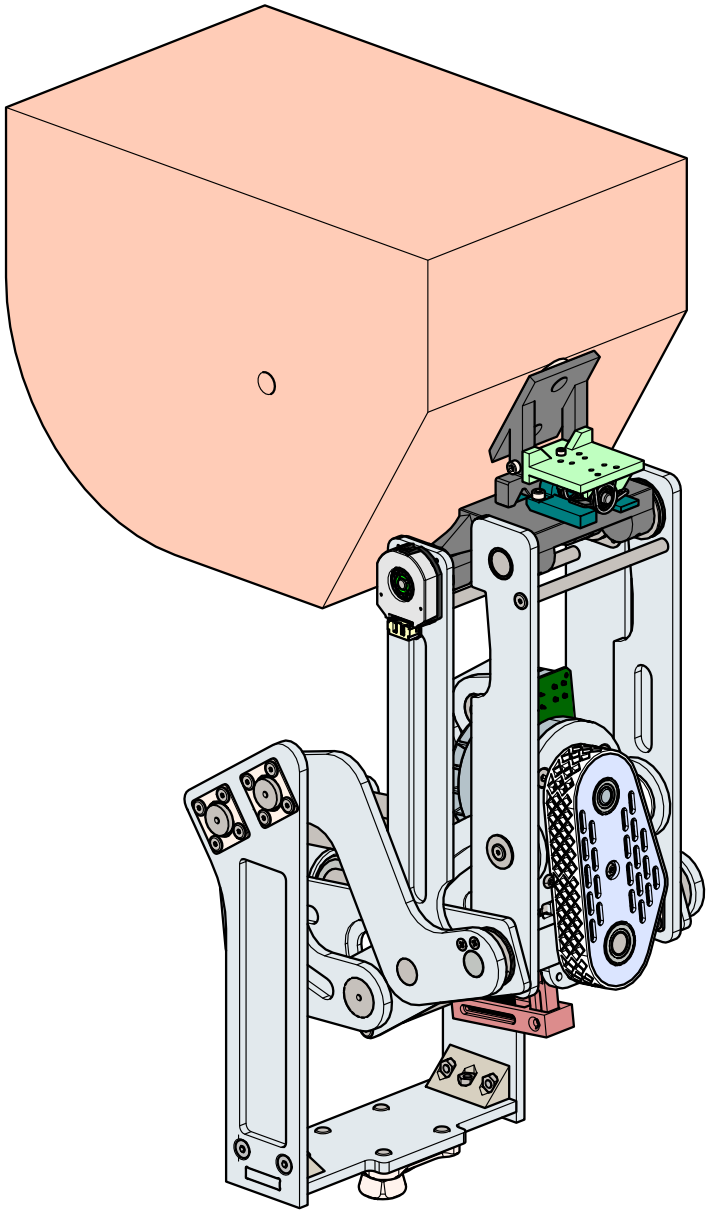

Figure 3.23: 3D view of the new base mounted on the prosthesis and attached to the (simplified) shell.

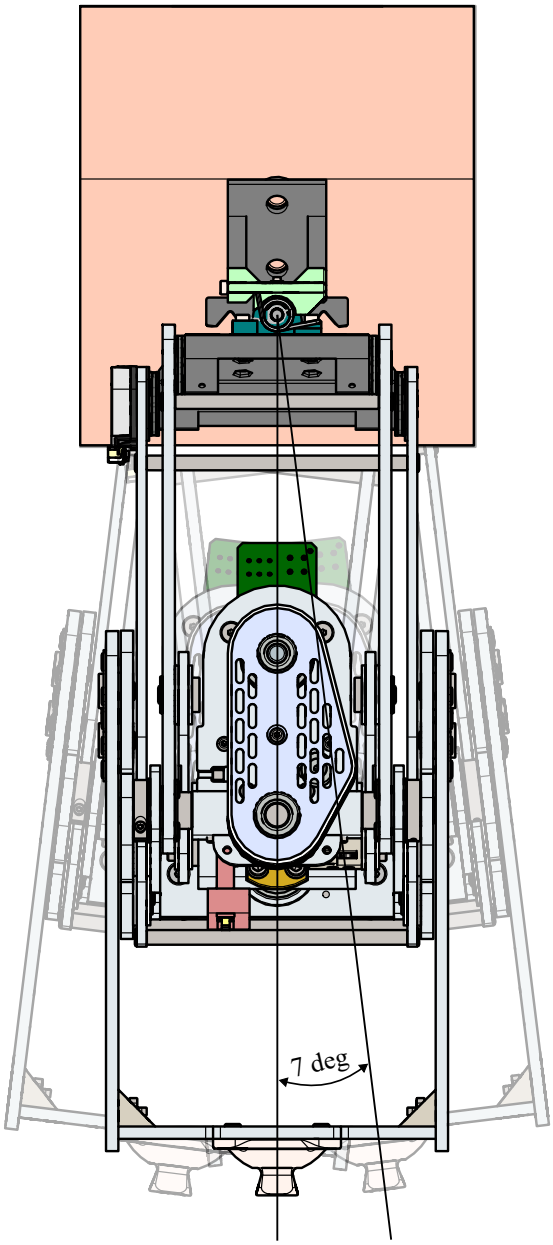


Figure 3.24: Front (Frontal plane) view of the re-designed base-prosthesis-shell assembly, showing the prosthesis in the standing position. Two extreme positions of the prosthesis in the frontal plane are shown semi-transparently.

## 3.5 Prototype

In this section, pictures of the assembled prototype are presented. Figure 3.25 shows the prototype from the front and from the side. These photographs can be compared to the CAD model in Figure 3.18.

Figure 3.26 provides a 3D view of the prototype, which can be compared to the CAD representation in Figure 3.17.

Figures 3.27, 3.28 and 3.29 show the prototype next to the original base from different angles, in order to observe the differences between the two parts.

Finally, Figure 3.30 shows the original base placed in front of the prototype, corresponding to Figure 3.19, to observe the extended portion in reality.

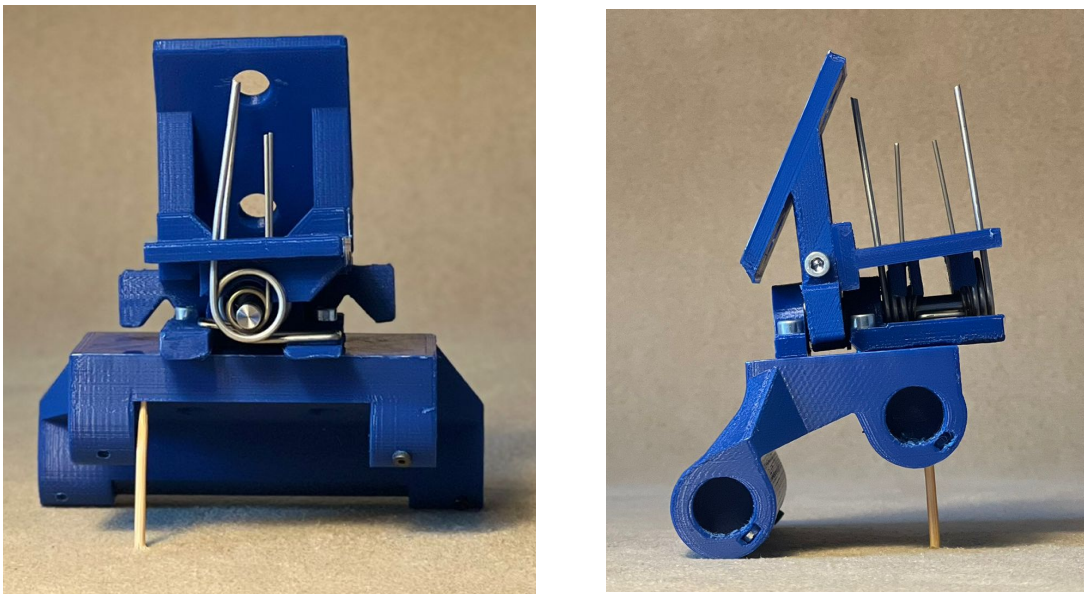

Figure 3.25: Front and side views of the 3D printed prototype. The toothpick is used to raise the front height to match de CAD views in section 3.4. Left : front view (frontal plane); right : side view (sagittal plane).

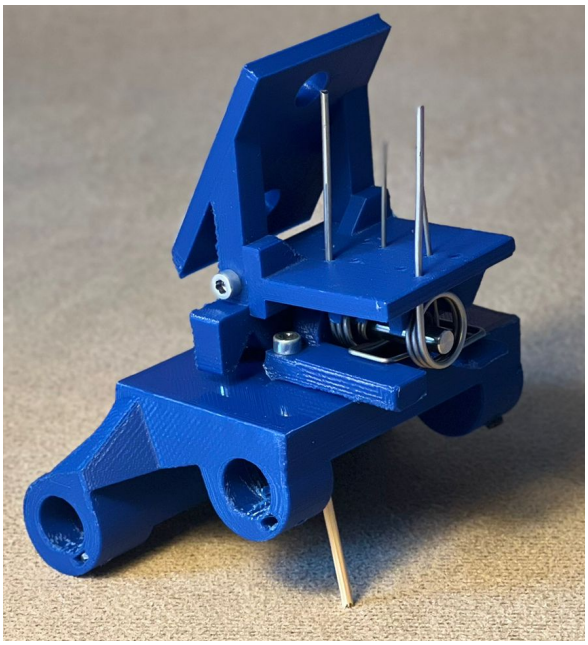

Figure 3.26: 3D view of the 3D printed prototype. The toothpick is used to raise the front height to match de CAD views in section 3.4.

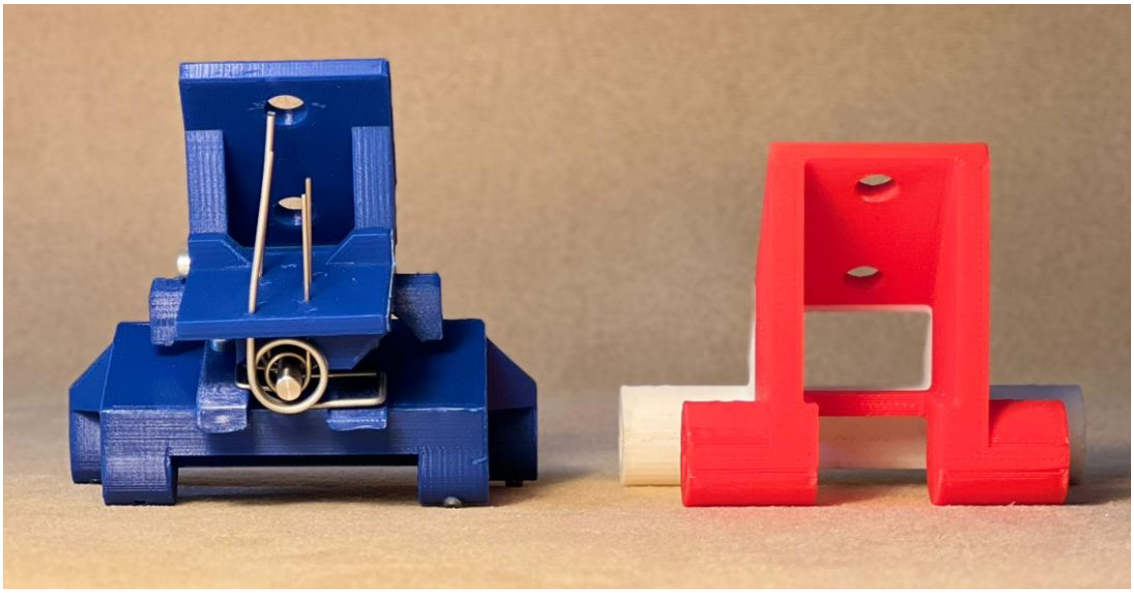

Figure 3.27: Front view (frontal plane) of the 3D printed re-designed base (blue) and the 3D printed original base (red and white) side by side.

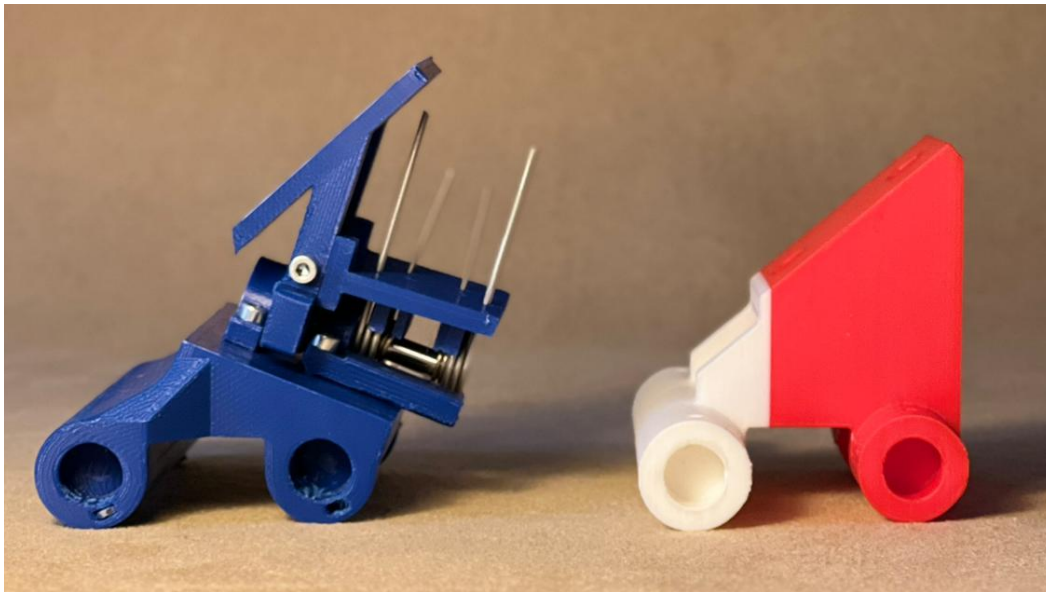

Figure 3.28: Side view (sagittal plane) of the 3D printed re-designed base (blue) and the 3D printed original base (red and white) side by side.

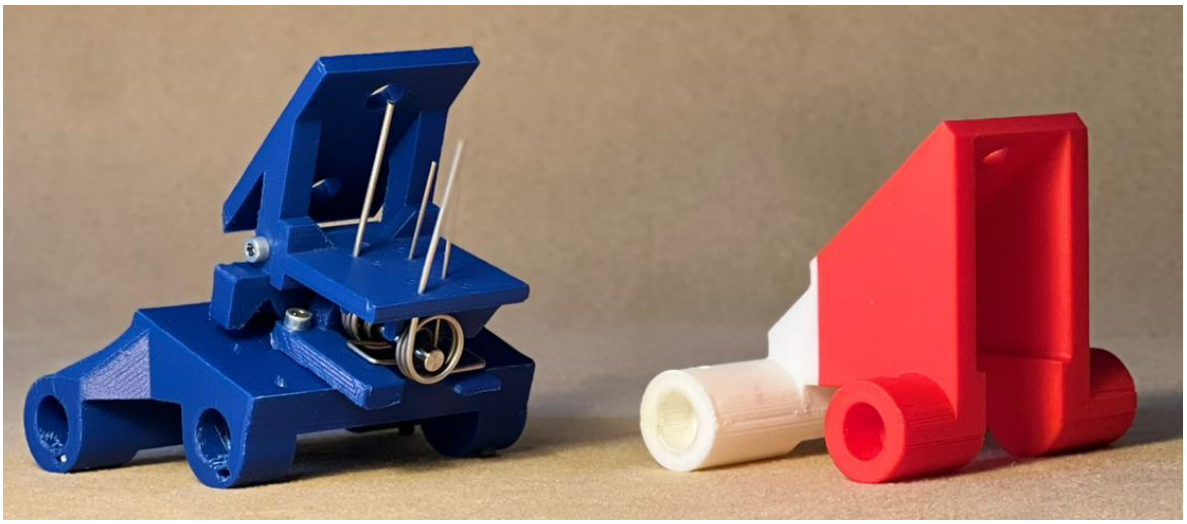

Figure 3.29: 3D view of the 3D printed re-designed base (blue) and the 3D printed original base (red and white) side by side.

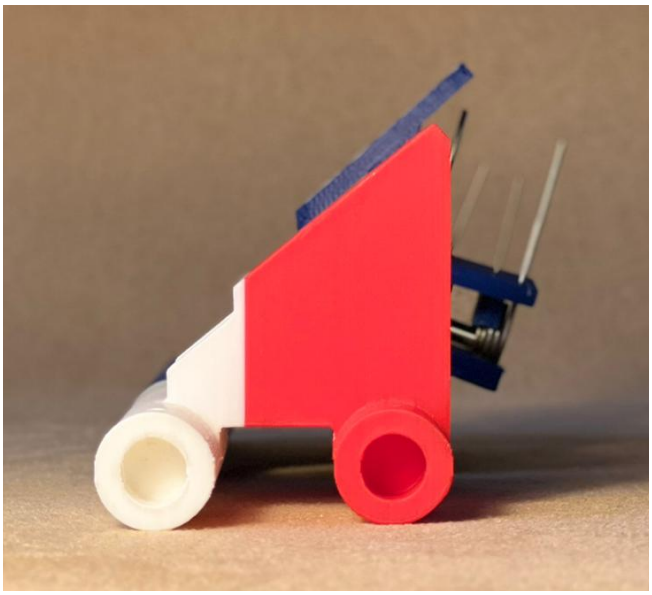

Figure 3.30: Picture of the overlay of the side view (sagittal plane) of the 3D printed original and the re-designed base.

# Chapter 4

# Validation of the prototype

This chapter presents the method used for validating the prototype and the expected outcomes of such a validation test. The experiment was not carried out due to the time constraints of the thesis, but a general methodology and the expected results are described here.

## 4.1 Methodology

The main objective of this validation is to verify the mechanical behavior of the prototype against the theoretical model presented in Figure 2.6 (Chapter 2). The methodology described here is inspired by the work in [43].

### 4.1.1 Experimental setup

The required equipment for this validation is shown in Figure 4.1.

First, a custom part is designed to secure the modified base. This part is fixed to a test bench using a bench vise, ensuring that the entire device remains stable when a force is applied. A custom 3D-printed part is inserted into the upper hole of the base. This part includes a hook to attach a dynamometer. An angle indicator is mounted on the spring-blocking part to measure the rotation of the upper section relative to the vertical axis. The dynamometer is then attached to the hook, and a horizontal force is applied manually. Under the small-angle assumption, a horizontal force can be considered perpendicular to the prosthesis.

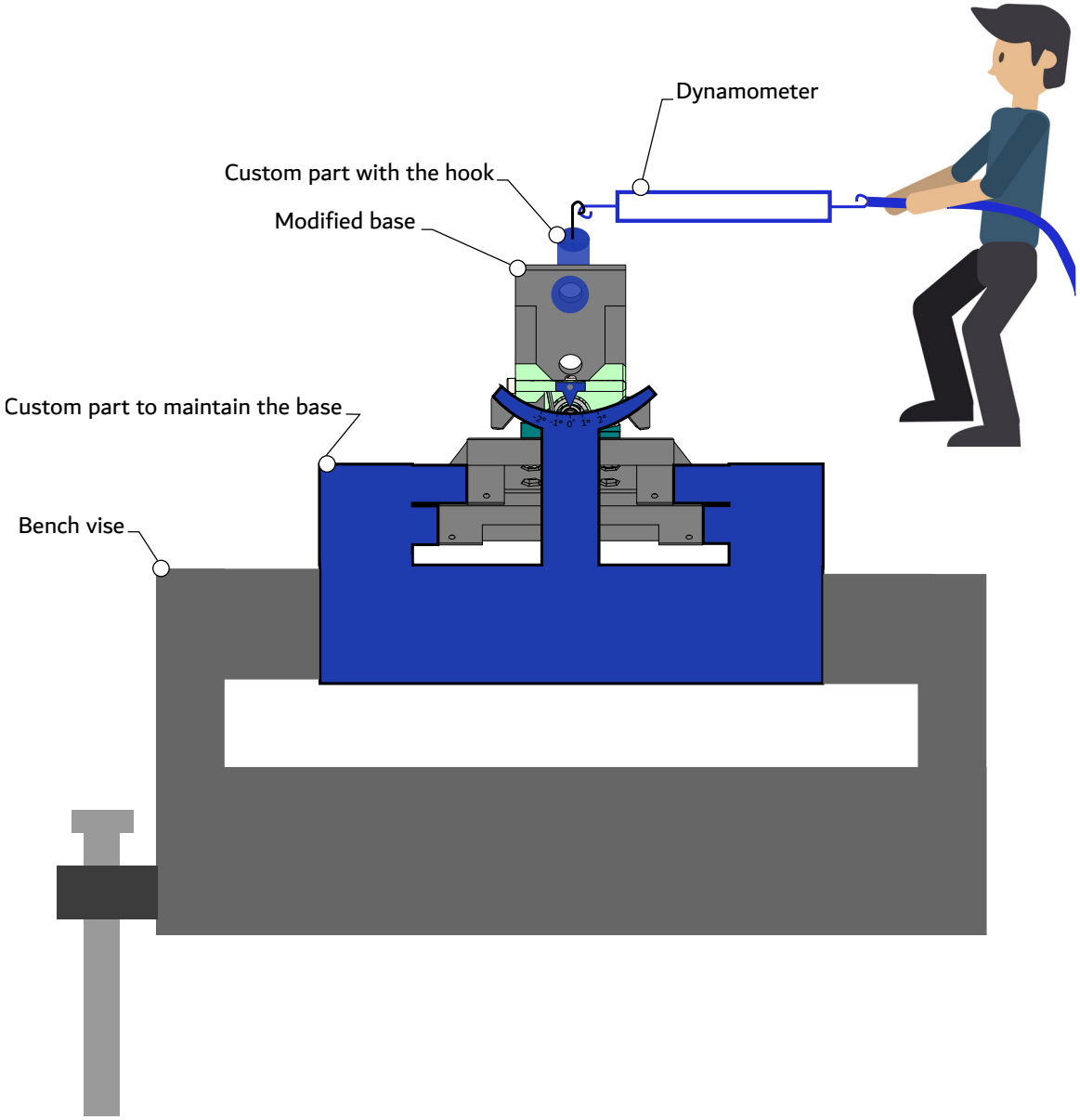


Figure 4.1: Schematic of the bench test for the experimental protocol.

### 4.1.2 Experimental protocol

The protocol starts by applying a horizontal force incrementally, from a minimum $F_{min}$ to a maximum $F_{max}$. For each force value, the corresponding angle $\theta$ is recorded using the angle indicator.

The test is performed on both sides of the prosthesis, with five repetitions for each force value and each side.

The moment at the rotation center is calculated as:

$$M = F \times d$$

where $d$ is the distance from the rotation axis to the point of force application.

The converted moments can be normalized by the theoretical mass associated with the springs. An average of the results is then calculated, along with the standard deviation.

### 4.1.3 Data analysis

From the experimental results, an angle–moment graph can be plotted. These data can be compared with the theoretical predictions from Chapter 2 using the relative error and the coefficient of determination $R^2$ to assess the linearity of the results. Repeatability can be evaluated by analyzing the variance between repetitions.

## 4.2 Expected results

The experimental angle–moment curves are expected to closely match the theoretical curves in Figure 2.6. Minor deviations may occur due to material compliance, friction, or measurement errors.

A successful validation would confirm that the prototype's mechanical behavior is representative of the linear approximation used in Chapter 2.

## 4.3 Further tests

Another possible experiment is to test the complete prosthesis–modified base assembly. For this, the adapter developed by L. Lhotellerie [43] can be used to collect angle and moment data during gait cycles on a treadmill. This approach allows testing with a person whose equivalent body mass associated with the spring is closer to the design requirements, without the need to find someone who has undergone hip disarticulation or hemipelvectomy.

These data can be processed using the same analysis tools described in the previous section (section 4.1). The results can then be expressed as angles and moments depending on the gait cycle percentage, as shown in Figures 1.4 and 1.5. This test would provide insights into the functional performance of the prosthesis in real-life situations.

# Chapter 5

# Conclusions and future work

To conclude this thesis, a summary of the work accomplished is provided, followed by an outlook for future developments.

## 5.1 Summary of the work

The thesis began with a brief motivation of the problem, highlighting the potential energy savings from a passive adduction/abduction implementation on an existing prosthesis. Such energy savings could increase the autonomy of people who have undergone hip disarticulation or hemipelvectomy by allowing them to walk longer distances with the same energy expenditure.

To give the reader a clear view of the challenges of this work, the biomechanics of the hip joint during walking gait were first explained, beginning with the gait cycle and then the mechanics of the hip joint.

A state-of-the-art review of hip disarticulation prostheses was carried out, examining both commercially available and prototype models. As no passive implementation of frontal plane movement exists for hip disarticulation prostheses, a review of ankle prostheses with passive frontal plane movement was also included.

The conclusion of the first chapter is that there is currently no research on passive implementation of abduction/adduction in the frontal plane for hip disarticulation prostheses. When this degree of freedom is implemented, it is done actively. Even for ankle prostheses, only a few works exist on passive inversion/eversion implementation. These observations were one of the main driving forces of this thesis.

To design this degree of freedom passively, springs were chosen as actuators. In order to achieve the goal as simply as possible, linear stiffness springs were selected. This choice led into the second chapter, which was dedicated to estimating the optimal linear stiffness of the hip in the frontal plane during walking. Data were collected, processed, and linear regressions were performed and compared. The conclusion was that the hip exhibits two different linear stiffness values in the frontal plane depending on the movement direction: adduction was found to be stiffer than abduction.

Once the stiffness values were estimated, the selection of the most suitable springs could be made, taking into account design constraints from the initial work of L. Devillez.

This selection process began by determining the necessary spring characteristics from the potential energy required according to the estimated stiffness. These results provided a lower limit for the energy storage capacity of the springs.

Spring data were extracted from the Inexal catalog for four different types: compression, tension, double torsion, and clock springs. After comparison, the double torsion spring emerged as the most suitable. The final step was selecting the specific double torsion spring to be used.

After choosing the spring type and defining the approximate morphology of the solution, the shaft has been dimensioned. Based on these values, the final design was produced.

Once the design was completed, the shaft, bearings, and springs were ordered from suppliers, and a 3D-printed prototype was assembled, as shown in the last part of Chapter 3.

To validate the prototype and verify the accuracy of the results, a validation protocol was designed and described in the final chapter. Although the test was not performed, the complete procedure was detailed, along with another proposed in-situ test for the modified base.

## 5.2 Future work

This thesis opens the way for further investigations in several areas.

The quality of the prototype could be improved by using machining techniques for the different parts composing the assembly in order to potentially reduce the friction losses. The blocking mechanism could also be redesigned for greater precision and safety. The spring alignment still presents some issues and could be improved by rethinking the way the constraints are applied to them.

Another important step is to perform the experimental validation of the existing prototype. As explained earlier, a test protocol has been developed but not yet carried out. This test could provide valuable information on the feasibility of the solution from a stability perspective, as well as the in-situ benefits or drawbacks of using a passive mechanism rather than an active one.

# Bibliography


[1] P. Yari, P. U. Dijkstra, and J. H. Geertzen, "Functional outcome of hip disarticulation and hemipelvectomy: A cross-sectional national descriptive study in the Netherlands," *Clinical Rehabilitation*, vol. 22, no. 12, pp. 1127–1133, Dec. 2008.

[2] S. M. Zaffer, R. L. Braddom, A. Conti, J. Goff, and D. Bokma, "TOTAL HIP DISARTICULATION PROSTHESIS WITH SUCTION SOCKET: Report of Two Cases: 1," *American Journal of Physical Medicine & Rehabilitation*, vol. 78, no. 2, p. 160, Mar. 1999.

[3] JD. WALDEN and DAVIS. BC, "PROSTHETIC FITTING AND POINTS OF REHABILITATION FOR HINDQUARTER AND HIP DISARTICULATION PATIENTS," *PROSTHETIC FITTING AND POINTS OF REHABILITATION FOR HINDQUARTER AND HIP DISARTICULATION PATIENTS*, 1979.

[4] R. D. McAnelly, M. Refaeian, D. G. O'Connell, G. D. Powell, and N. E. Walsh, "Successful prosthetic fitting of a 73-year-old hip disarticulation amputee patient with cardiopulmonary disease," *Archives of Physical Medicine and Rehabilitation*, vol. 79, no. 5, pp. 585–588, May 1998.

[5] Z. H. Wool and S. D. Messinger, "Labors of Love: The Transformation of Care in the Non-Medical Attendant Program at Walter Reed Army Medical Center," *Medical Anthropology Quarterly*, vol. 26, no. 1, pp. 26–48, 2012.

[6] N. Kumar and B. Gupta, "Global incidence of primary malignant bone tumors," *Current Orthopaedic Practice*, vol. 27, no. 5, p. 530, September/October 2016.

[7] F. Nowroozi, M. L. Salvanelli, and L. H. Gerber, "Energy expenditure in hip disarticulation and hemipelvectomy amputees," *Archives of physical medicine and rehabilitation*, vol. 64, no. 7, pp. 300–303, Jul. 1983.

[8] A. Alili, A. Fleming, V. Nalam, M. Liu, J. Dean, and H. Huang, "Abduction/Adduction Assistance From Powered Hip Exoskeleton Enables Modulation of User Step Width During Walking," *IEEE Transactions on Biomedical Engineering*, vol. 71, no. 1, pp. 334–342, Jan. 2024.

[9] A. Kharb, V. Saini, Y. K. Jain, and S. Dhiman, "A REVIEW OF GAIT CYCLE AND ITS PARAMETERS," vol. 13, 2011.

[10] W. Pirker and R. Katzenschlager, "Gait disorders in adults and the elderly," *Wiener klinische Wochenschrift*, vol. 129, no. 3, pp. 81–95, Feb. 2017.

[11] M. Sangeux, "Biomechanics of the Hip During Gait," in *The Pediatric and Adolescent Hip: Essentials and Evidence*, S. Alshryda, J. J. Howard, J. S. Huntley, and J. G. Schoenecker, Eds. Cham: Springer International Publishing, 2019, pp. 53–71.

[12] "Movement about Joints, Part 5: The Hip," https://www.crossfit.com/essentials/movement-about-joints-part-5-the-hip.

[13] "These Are the Anatomical Directional Terms You Should Know," https://www.thoughtco.com/anatomical-directional-terms-and-body-planes-373204.

[14] O. Skalshøi, C. H. Iversen, D. B. Nielsen, J. Jacobsen, I. Mechlenburg, K. Søballe, and H. Sørensen, "Walking patterns and hip contact forces in patients with hip dysplasia," *Gait & Posture*, vol. 42, no. 4, pp. 529–533, Oct. 2015.

[15] N. B. Reese and W. D. Bandy, *Joint Range of Motion and Muscle Length Testing - E-Book: Joint Range of Motion and Muscle Length Testing - E-Book*. Elsevier Health Sciences, Mar. 2016.

[16] D. Hara, Y. Nakashima, S. Hamai, H. Higaki, S. Ikebe, T. Shimoto, M. Hirata, M. Kanazawa, Y. Kohno, and Y. Iwamoto, "Kinematic Analysis of Healthy Hips during Weight-Bearing Activities by 3D-to-2D Model-to-Image Registration Technique," *BioMed Research International*, vol. 2014, no. 1, p. 457573, 2014.

[17] P. Adam, L. Béguin, S. Grosclaude, B. Jobard, and M.-H. Fessy, "[Functional range of motion of the hip joint]," *Revue de chirurgie orthopedique et reparatrice de l'appareil moteur*, vol. 94, no. 4, pp. 382–391, Jun. 2008.

[18] C. A. McLAURIN, "The Evolution of the Canadian-Type Hip-Disarticulation Prosthesis."

[19] T. Van der Waarde, "Ottawa experience with hip disarticulation prostheses," *Prosthetics and orthotics international*, vol. 38, pp. 29–33, 1984.

[20] S. Mroz, "Design and Prototype Validation of a Laterally Mounted Powered Hip Joint for Hip Disarticulation Prostheses," Ph.D. dissertation, Université d'Ottawa / University of Ottawa, May 2023.

[21] N. Hata, T. Kubo, and t. INOUE, "Development of a powered hip disarticulation prosthesis with swing phase controller," *ResearchGate*.

[22] D. Langlois, "(71) Applicant: Össur hf, Reykjavík (IS)."

[23] Y. Ueyama, K. , Tsutomu, and M. and Shibata, "Robotic hip-disarticulation prosthesis: Evaluation of prosthetic gaits in a non-amputee individual," *Advanced Robotics*, vol. 34, no. 1, pp. 37–44, Jan. 2020.

[24] S. Luo, X. Shu, H. Zhu, and H. Yu, "Design and optimization of a new integrated hip and knee prosthesis structure," *Artificial Organs*, vol. 48, no. 1, pp. 50–60, 2024.

[25] K. Brannen, "DESIGN AND EVALUATION OF A MICROPROCESSOR-CONTROLLED POWERED HIP PROSTHESIS."

[26] L. Devillez, B. Herman, and R. Ronsse, "Design of a Compact Active Hip Prosthesis with Human-Like Range of Motion and Torque*," in *2024 10th IEEE RAS/EMBS International Conference for Biomedical Robotics and Biomechatronics (BioRob)*, Sep. 2024, pp. 160–166.

[27] T. Schoppen, A. Boonstra, J. W. Groothoff, J. de Vries, L. N. H. Göeken, and W. H. Eisma, "Employment status, job characteristics, and work-related health experience of people with a lower limb amputation in The Netherlands," *Archives of Physical Medicine and Rehabilitation*, vol. 82, no. 2, pp. 239–245, Feb. 2001.

[28] V. B.s., T. Thinlay, S. K. Jayswal, S. Pradeep, M. Bais, K. D. Prasad, and J. I. P. Singh, "Design and structural analysis of a passive ankle-foot prosthesis with manually adjustable stiffness and having two degrees of freedom," *Materials Today: Proceedings*, vol. 65, pp. 3496–3505, Jan. 2022.

[29] H.-T. Pham, M.-N. Le, and V.-T. Mai, "A Novel Multi-Axis Compliant Prosthetic Ankle Foot to Support the Rehabilitation of Amputees," in *2016 3rd International Conference on Green Technology and Sustainable Development (GTSD)*, Nov. 2016, pp. 238–243.

[30] E. J. Rouse, R. D. Gregg, L. J. Hargrove, and J. W. Sensinger, "The Difference between Stiffness and Quasi-stiffness in the Context of Biomechanical Modeling," *IEEE transactions on bio-medical engineering*, vol. 60, no. 2, pp. 562–568, Feb. 2013.

[31] China Top CNC Machining Service OEM Supplier & Manufacturer | Junying. [Online]. Available: https://www.cnclathing.com/

[32] T. F. Besier, D. L. Sturnieks, J. A. Alderson, and D. G. Lloyd, "Repeatability of gait data using a functional hip joint centre and a mean helical knee axis," *Journal of Biomechanics*, vol. 36, no. 8, pp. 1159–1168, Aug. 2003.

[33] J.-P. Kulmala, M. T. Korhonen, S. Kuitunen, H. Suominen, A. Heinonen, A. Mikkola, and J. Avela, "Whole body frontal plane mechanics across walking, running, and sprinting in young and older adults," *Scandinavian Journal of Medicine & Science in Sports*, vol. 27, no. 9, pp. 956–963, 2017.

[34] A. G. McMillan, A. M. E. Pulver, D. N. Collier, and D. S. B. Williams, "Sagittal and frontal plane joint mechanics throughout the stance phase of walking in adolescents who are obese," *Gait & Posture*, vol. 32, no. 2, pp. 263–268, Jun. 2010.

[35] F. Molina-Rueda, I. M. Alguacil-Diego, A. Cuesta-Gómez, J. Iglesias-Giménez, A. Martín-Vivaldi, and J. C. Miangolarra-Page, "Thorax, pelvis and hip pattern in the frontal plane during walking in unilateral transtibial amputees: Biomechanical analysis," *Brazilian Journal of Physical Therapy*, vol. 18, pp. 252–258, 2014-May-Jun.

[36] Graphreader.com - Online tool for reading graph image values and save as CSV / JSON. [Online]. Available: https://www.graphreader.com/

[37] G. Pahl and W. Beitz, *Engineering Design: A Systematic Approach*. Springer Science & Business Media, Nov. 2013.

[38] M. O. Karaca, E. A. Özbek, M. Özyıldıran, A. Merter, K. Başarır, H. Y. Yıldız, and Y. Sağlık, "External and internal hemipelvectomy: A retrospective analysis of 68 cases," *Joint Diseases and Related Surgery*, vol. 33, no. 1, pp. 132–141, Mar. 2022.

[39] "EASA review of standard passenger weights in 2022 shows no significant change | EASA," https://www.easa.europa.eu/en/newsroom-and-events/news/easa-review-standard-passenger-weights-2022-shows-no-significant-change, Nov. 2022.

[40] R. C. Juvinall and K. M. Marshek, *Fundamentals of Machine Component Design*. John Wiley & Sons, Jun. 2020.

[41] J. Nilsson and A. Thorstensson, "Ground reaction forces at different speeds of human walking and running," *Acta Physiologica Scandinavica*, vol. 136, no. 2, pp. 217–227, 1989.

[42] C. K. Wong, M. S. Rissland, D. M. Madagan, and K. N. Jones, "A Scoping Review of Physical Activity in People With Lower-Limb Loss: 10,000 Steps Per Day?" *Physical Therapy*, vol. 101, no. 8, p. pzab115, Aug. 2021.

[43] L. Lhotellerie, "Bionic prosthesis for the lower-limb : adapter for testing a full leg prosthesis," https://hdl.handle.net/2078.2/32308.

# Artificial intelligence declaration

This document attests the use of generative AI for this work.

Copilot has been used to help to code and accelerate the work flow. ChatGPT has been used to correct grammar and spelling, generates around 20 % of the code lines and to search for certain sources.

Signature :

Hugo Duvivier

# Appendix A

# G. Pahl and W. Beitz steps for engineering design

The method described in [37] provides a systematic and structured approach to mechanical design. The main steps are:

- Clarification of the task, which includes defining the specifications.
- Conceptual design.
- Embodiment design.
- Detail design.

In this chapter, only the clarification of the task and conceptual design are detailed. The other steps are covered in the main body of the thesis in Chapter 3.

## A.1 Specifications

This section presents the specifications established at the beginning of the thesis. The aim is to identify the main functions and requirements, ensuring clarity on the project objectives.

## Functions

F1 : Allow abduction/adduction movement on existing prosthesis

## Functionnal requirement

FR 1.1 : Ensure 7-degree range of motion

FR 1.2 : Choice of stiffness for use and return to steady state

FR 1.3 : 0 degree locking of the mechanism

## Constraints

C2 : Must be adapted to the existing prosthesis of L.Devillez

C3 : Guaranteed safe operation in all circumstances (safety)

## Constraint requirement

CR 2.1 : Can only change one part on the existing constraint to respect its cdc.

CR 2.2 : Must be able to adapt to the user's morphology and desire for stiffness

CR 3.1 : Stability: maintaining balance when walking and changing posture

CR 3.2 : Backup mechanism in case of failure

## A.2 Conceptual design

### A.2.1 Graph of objectives

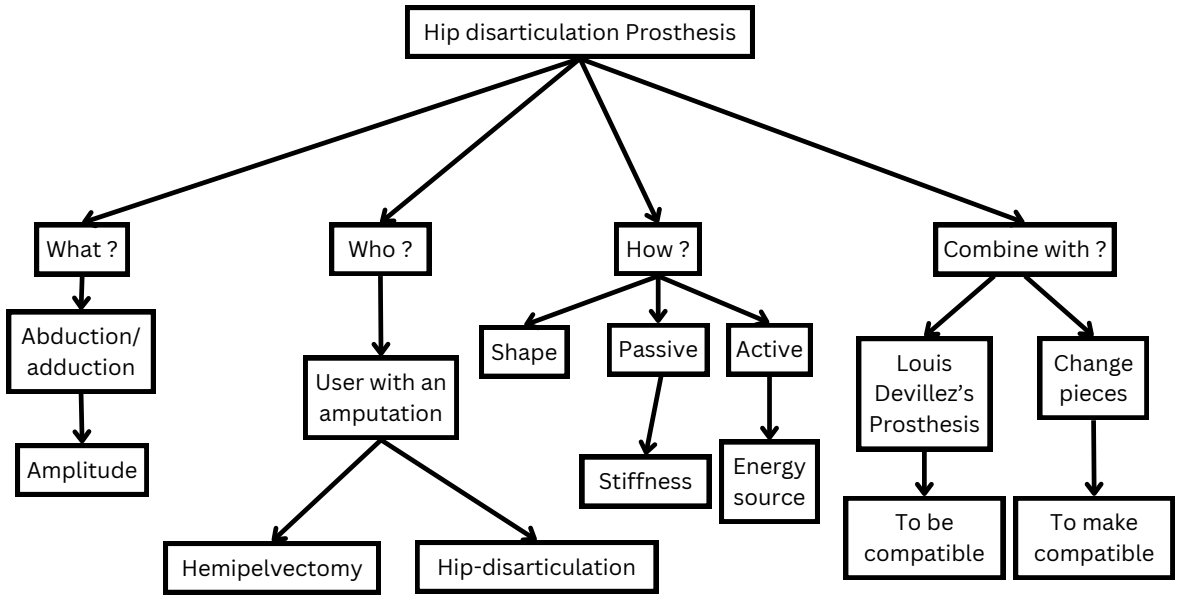


Figure A.1: Graph of objectives of the master thesis.

### A.2.2 Graph of functions

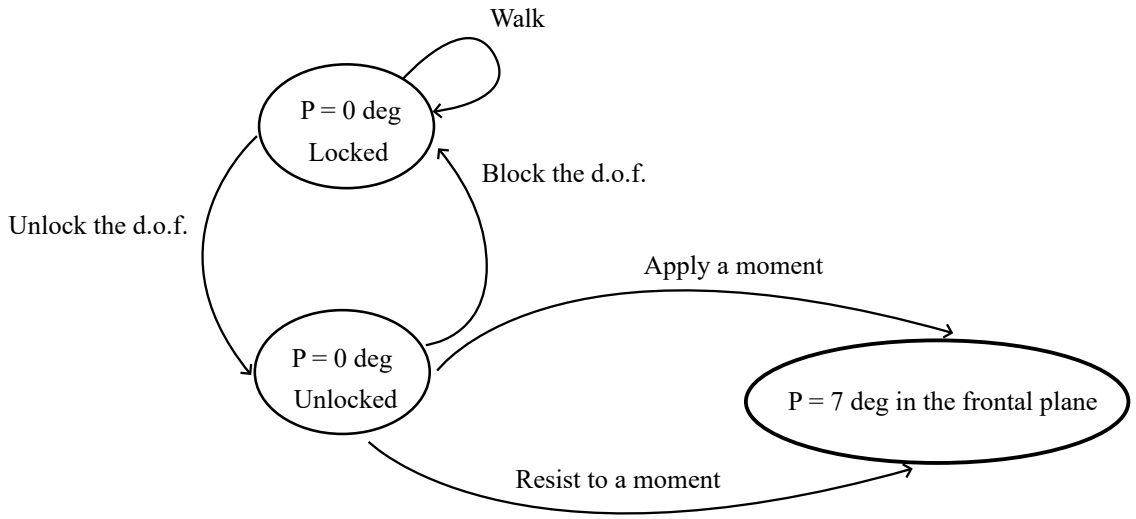


Figure A.2: Graph of functions of the project. $P$ represents the angle between the prosthesis and the vertical axis.

### A.2.3 Morphological chart

This subsection focuses on the morphological chart, which is used to explore possible solutions for each function of the mechanism.

# Morphological table

## Blocking the D.O.F

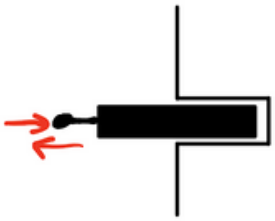
Pin

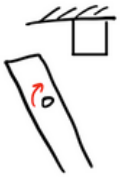
Limit stop

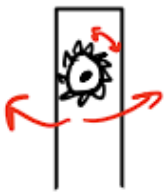
Brakes/Friction

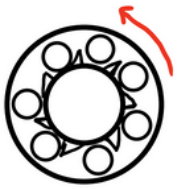
One Way bearing

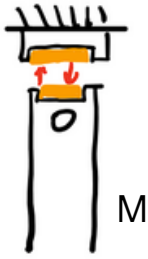
Magnets

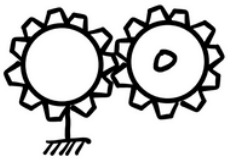
Fixed gear

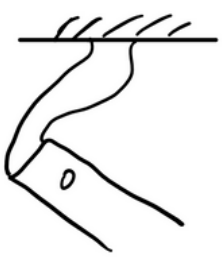
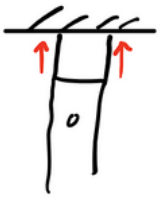
Fastened cables

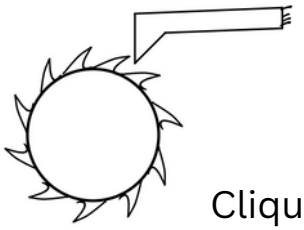
Cliquet

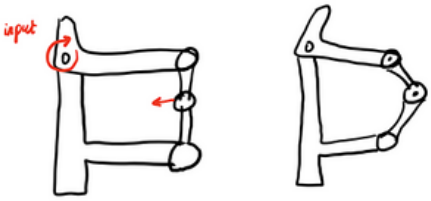

Singularity

## Actuation of the D.O.F

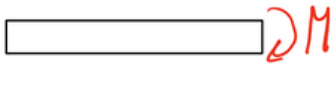

Torsion bar

Helical compression

Helical tension

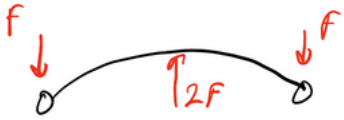

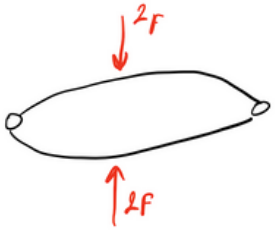

Beam spring

Spiral torsion

Helical torsion

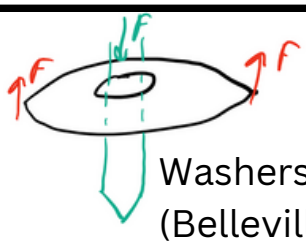

Washers (Belleville)

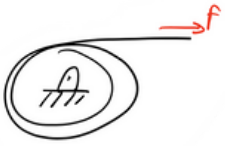

Constant force

Pneumatic

Magnetic

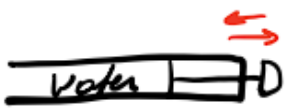
Hydraulic spring

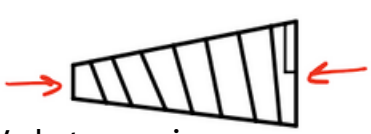
Volute spring

**Guiding the D.O.F**

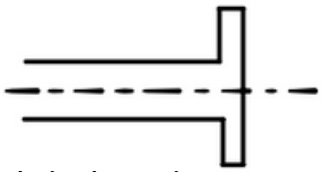

Plain bearing

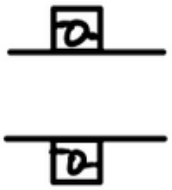

Bearing

Friction

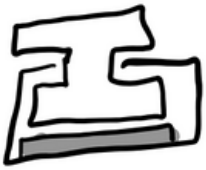

Linear rolling

Magnetic

**Transmission**

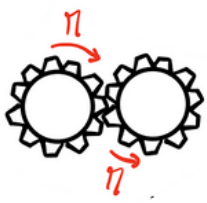

Gears

Coupling shaft

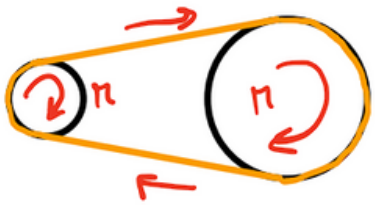

Belt/Chains

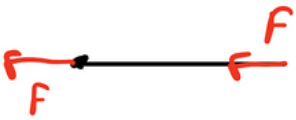

Cables

Magnets

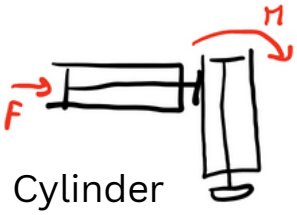

Cylinder

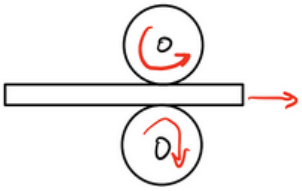

Friction

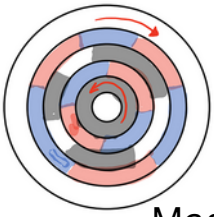

Magnetic bearing

### A.2.4 Concept variants

This subsection presents the drawings of the concept variants. These were generated before any stiffness calculations, so the designs remain general. Six variants are represented here, with features derived from the morphological chart.

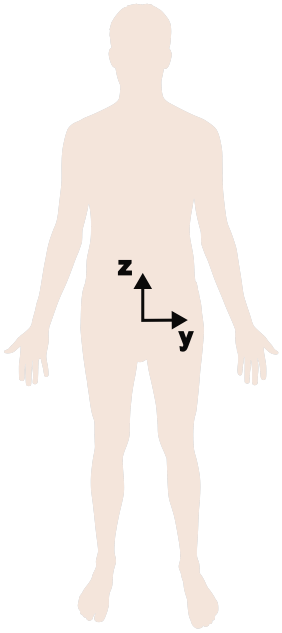


# V1 : Two sides springs

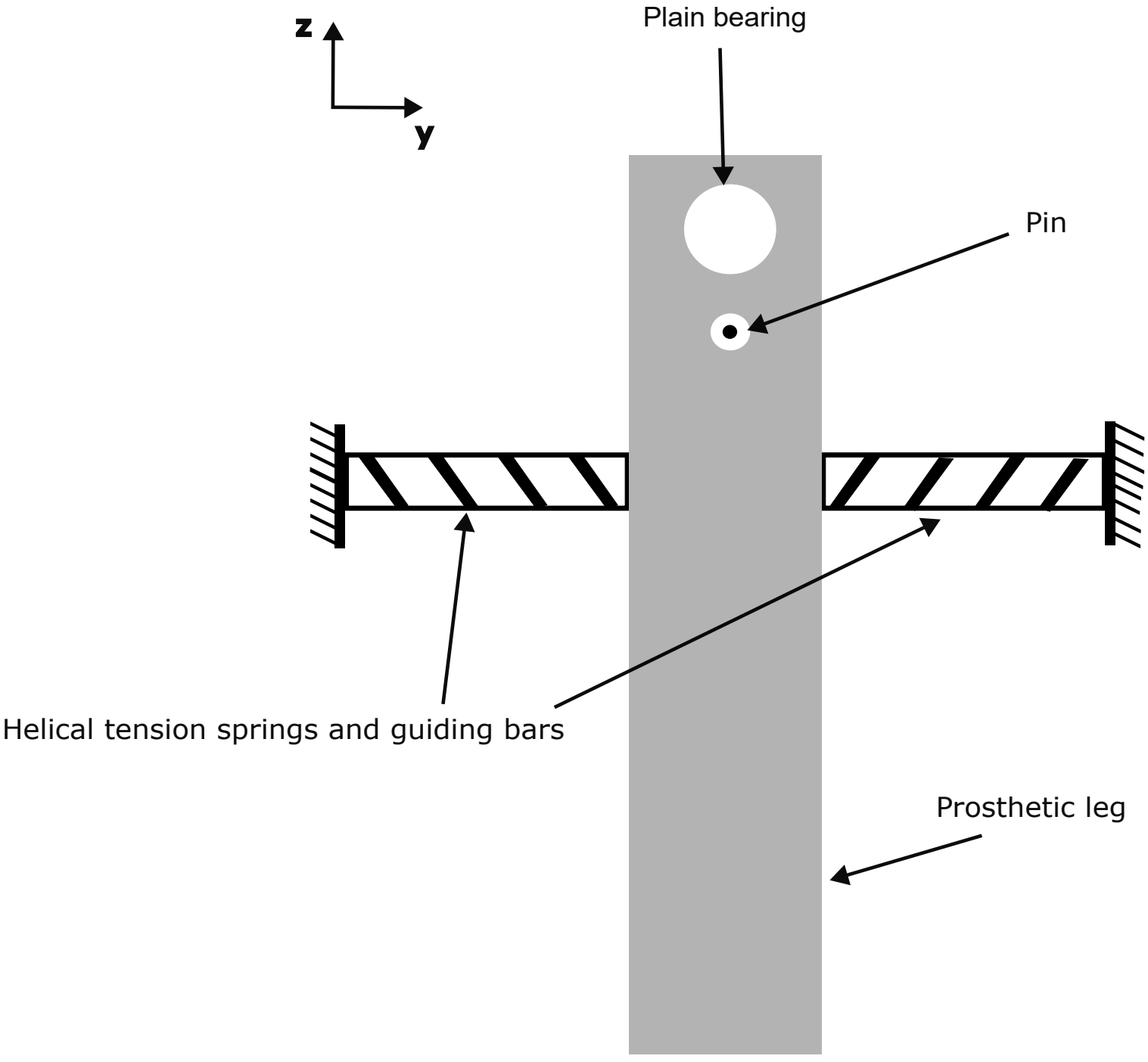

# V2 : Spiral Springs

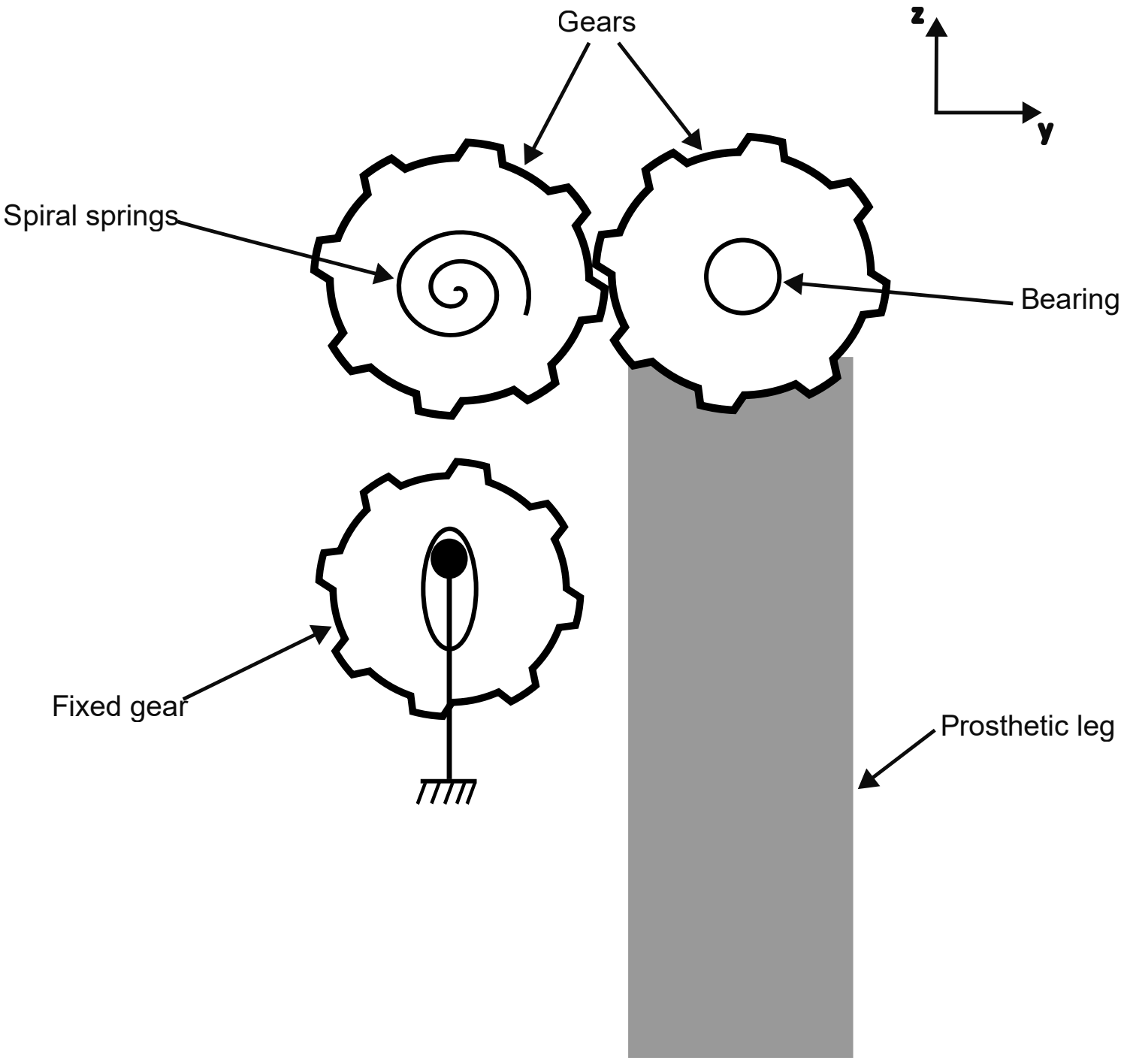

# V3 : Torsion spring

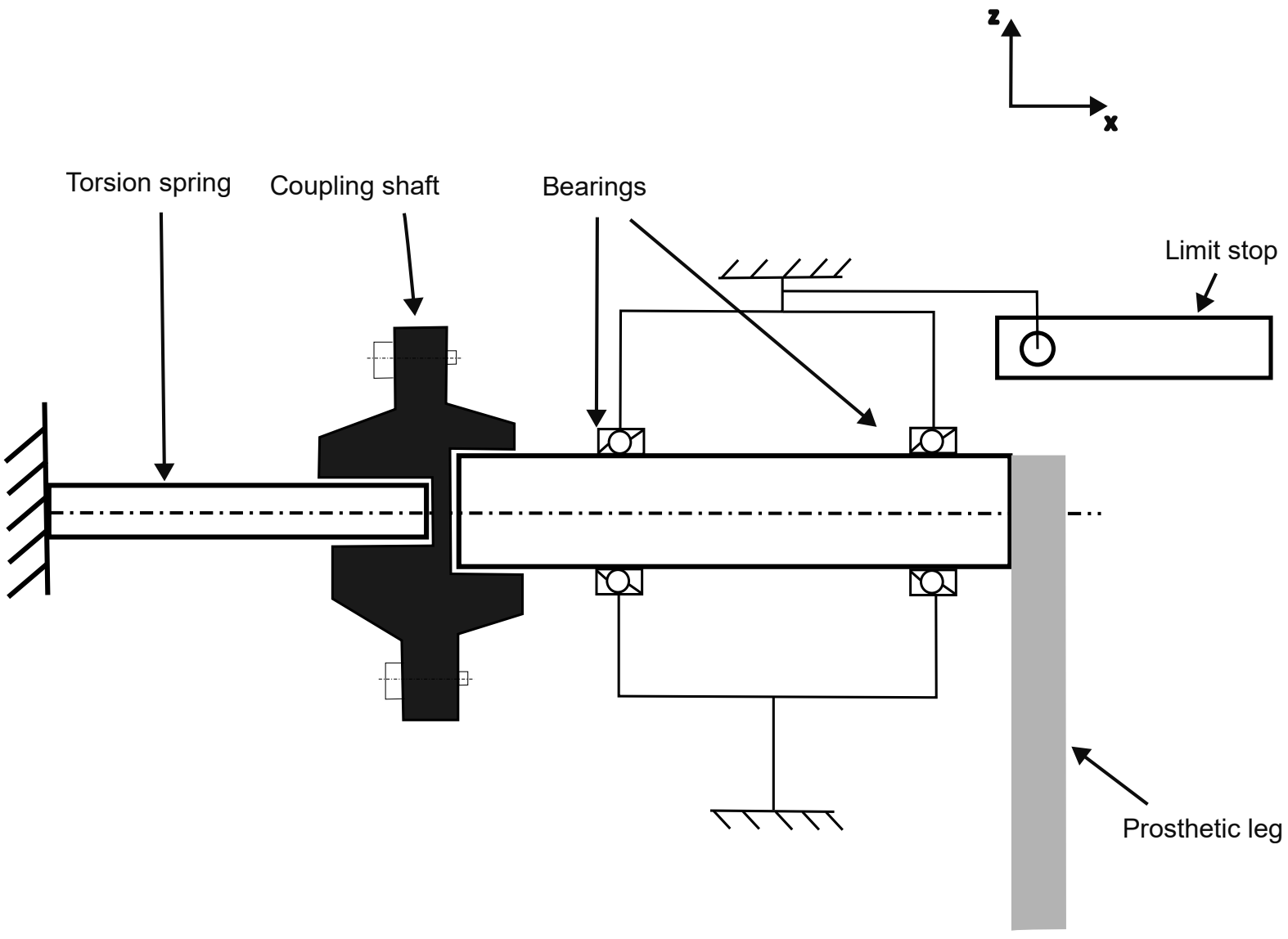

# V4 : Camshaft

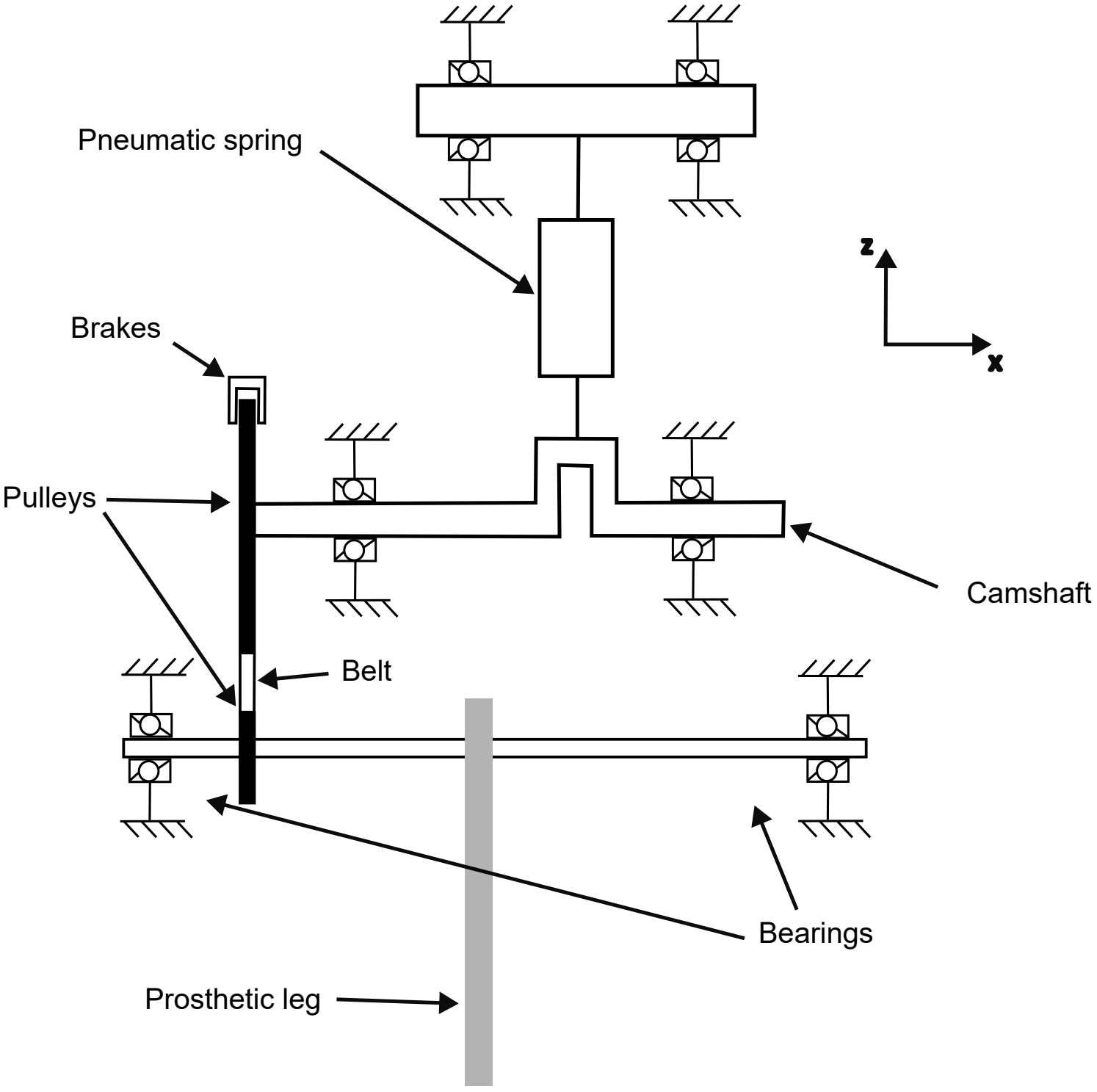
Pneumatic spring
Brakes
Pulleys
Belt
Camshaft
Bearings
Prosthetic leg
z
x

# V5 : Rack and pignon

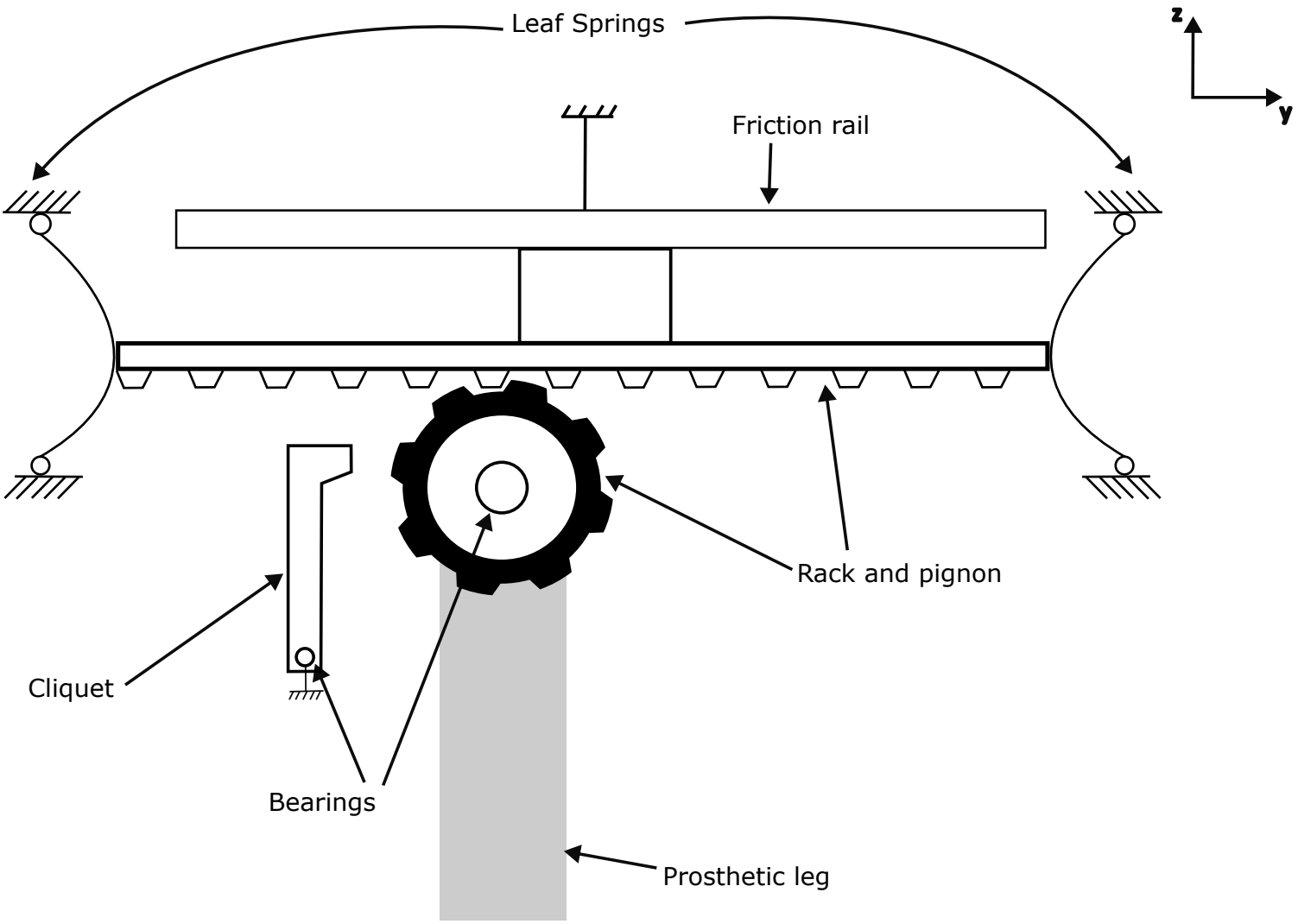

# V6 : Without rotation

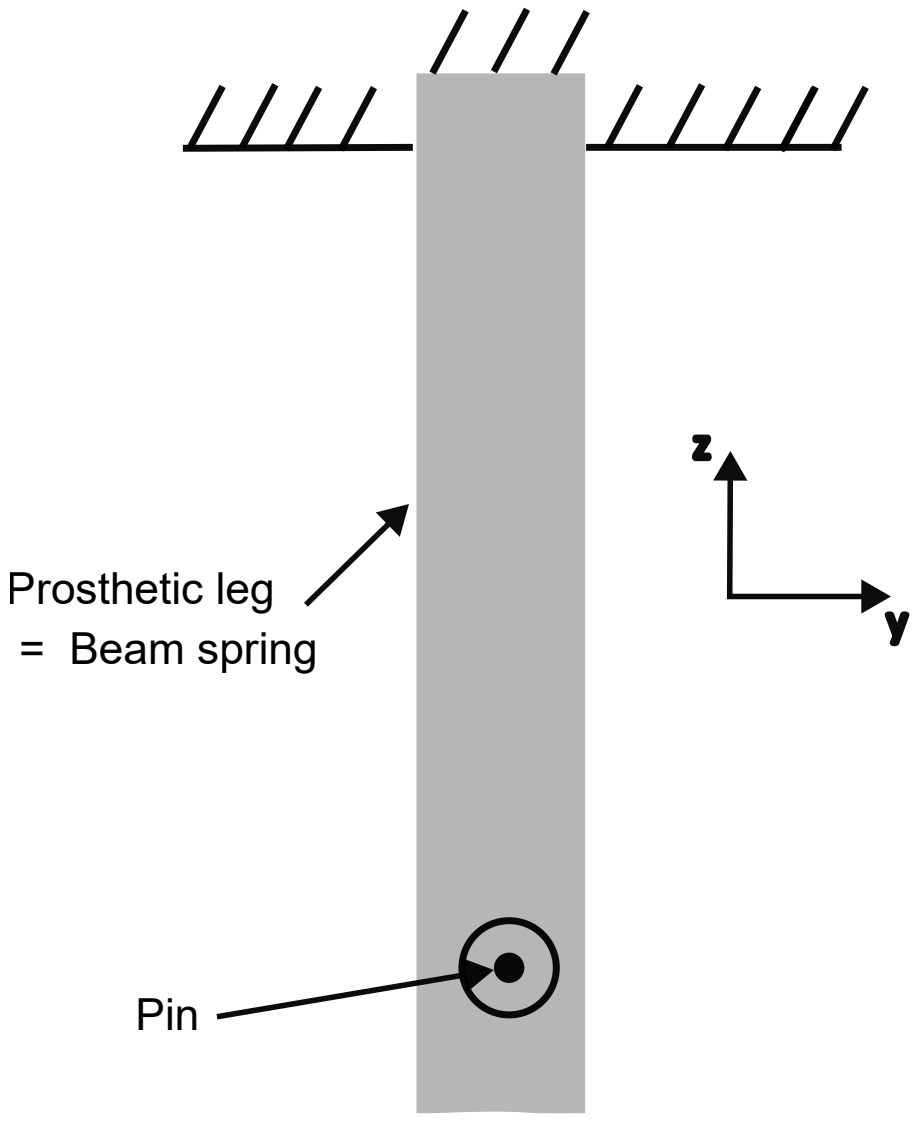

# Appendix B

# The $\alpha$ parameter

To determine a valid range of springs, the selection criterion is the potential energy a spring can store. The minimum value corresponds to the energy required for the application (e.g., hip movement in the frontal plane), while the maximum value is determined by the $\alpha$ parameter. This coefficient, greater than 1, multiplies the required energy:

$$E_{max,interval} = \alpha \times E_{required}$$

The purpose of $\alpha$ is to filter out springs that are too stiff for the application.

An example of a valid interval for selected springs is shown in Figure B.1.

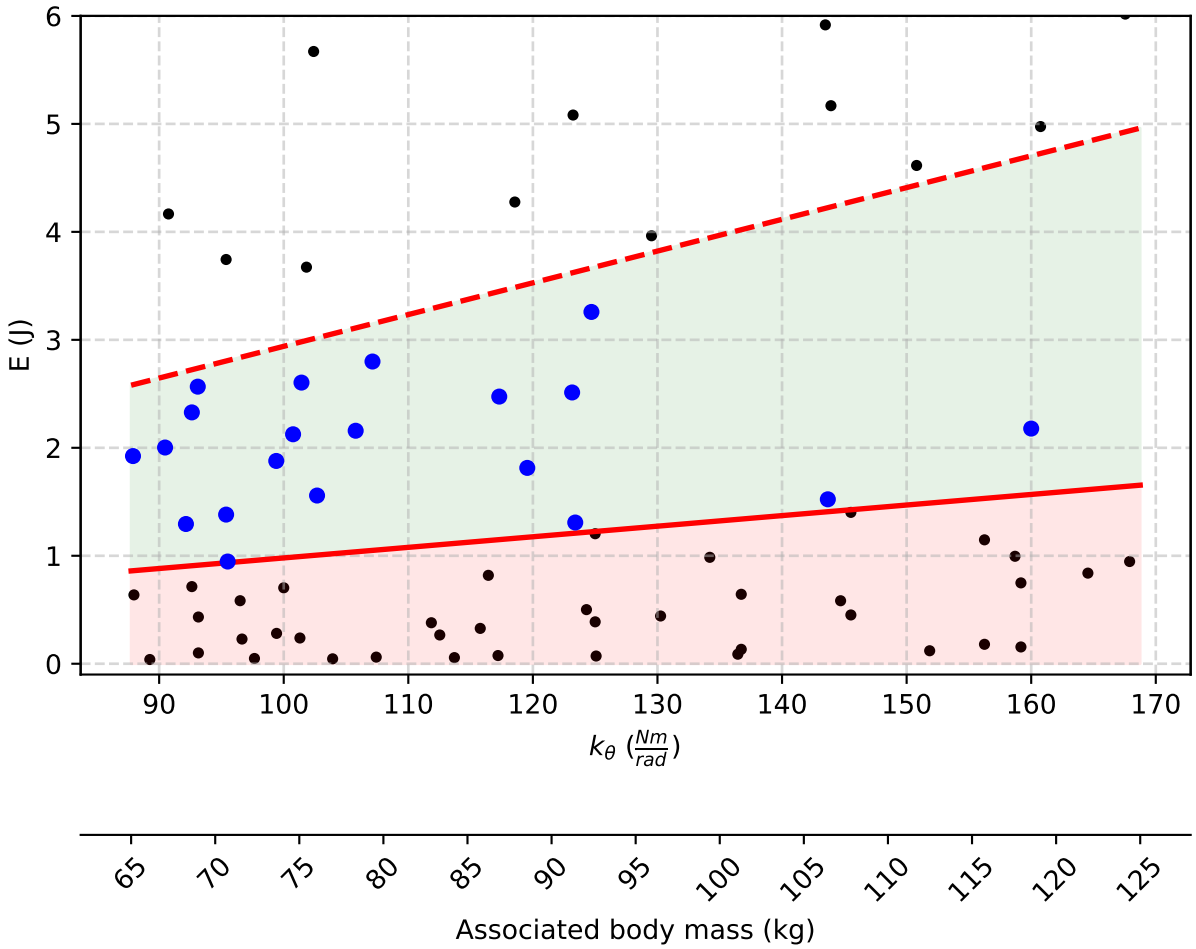


Figure B.1: Example of valid energy interval for compression springs in the abduction movement with $\alpha = 3$. Solid ed line : required energy; dashed red line : required energy multiplied by $\alpha$; black points : springs not in the interval; blue points : valid springs in the interval

To compare spring families, the maximum $\alpha$ must be determined for each family. The limiting factor is the largest spring length $L_m$. The maximum $\alpha$, $\alpha_{max}$, is chosen so that the mean $L_m$ of the springs in the interval remains below 100 mm. This ensures compatibility with the design constraints. Results are summarized in Table B.1. Since the double torsion springs never exceed 100 mm, no maximum $\alpha$ is needed for this family.

Table B.1: Maximum value of $\alpha_{max}$ for each spring family.

| Spring family | Compr-ession | Traction | Double torsion | Clock | Parallel compres-sion | Parallel traction |
|---|---|---|---|---|---|---|
| $\alpha_{max}$ | 10 | 10 | / | 5000 | 10 | 3 |

With $\alpha$ defined, the mean $\Delta k_{max}$ and $L_m$ can be calculated for each spring family. Figure B.2 illustrates the method for compression springs.

Figure B.3 and B.4 allows comparing the evolution of $L_m$ and $\Delta k_{max}$ for every spring family. This highlights the thoughtful choice of compression springs to minimize the clutter of the assembly.

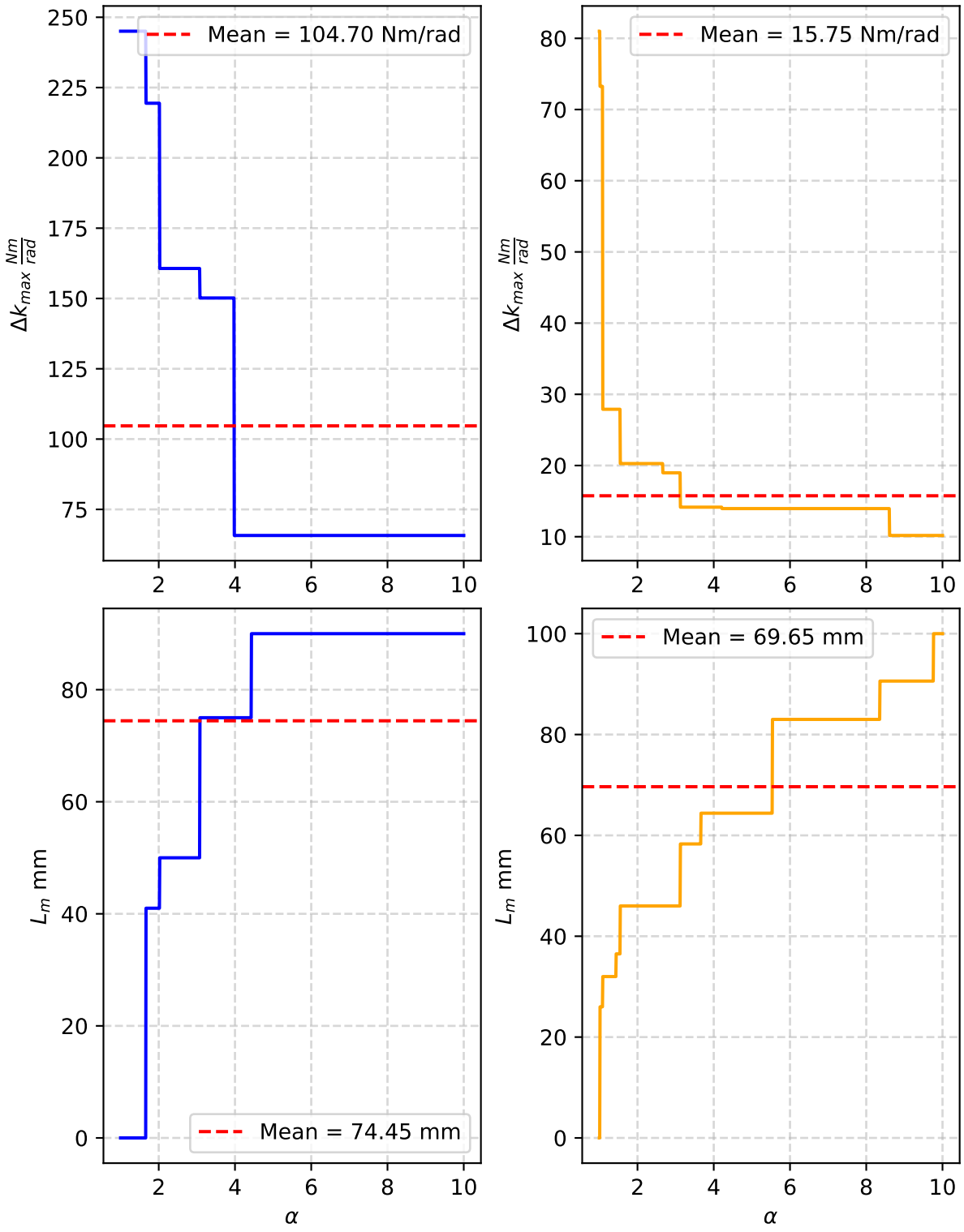


Figure B.2: $\Delta k_{max}$ and $L_m$ across the interval $\alpha = 1$ to $\alpha = \alpha_{max}$. Blue lines : adduction values; yellow lines : abduction values; dashed red line : mean across the $\alpha$ interval used to compare spring families.

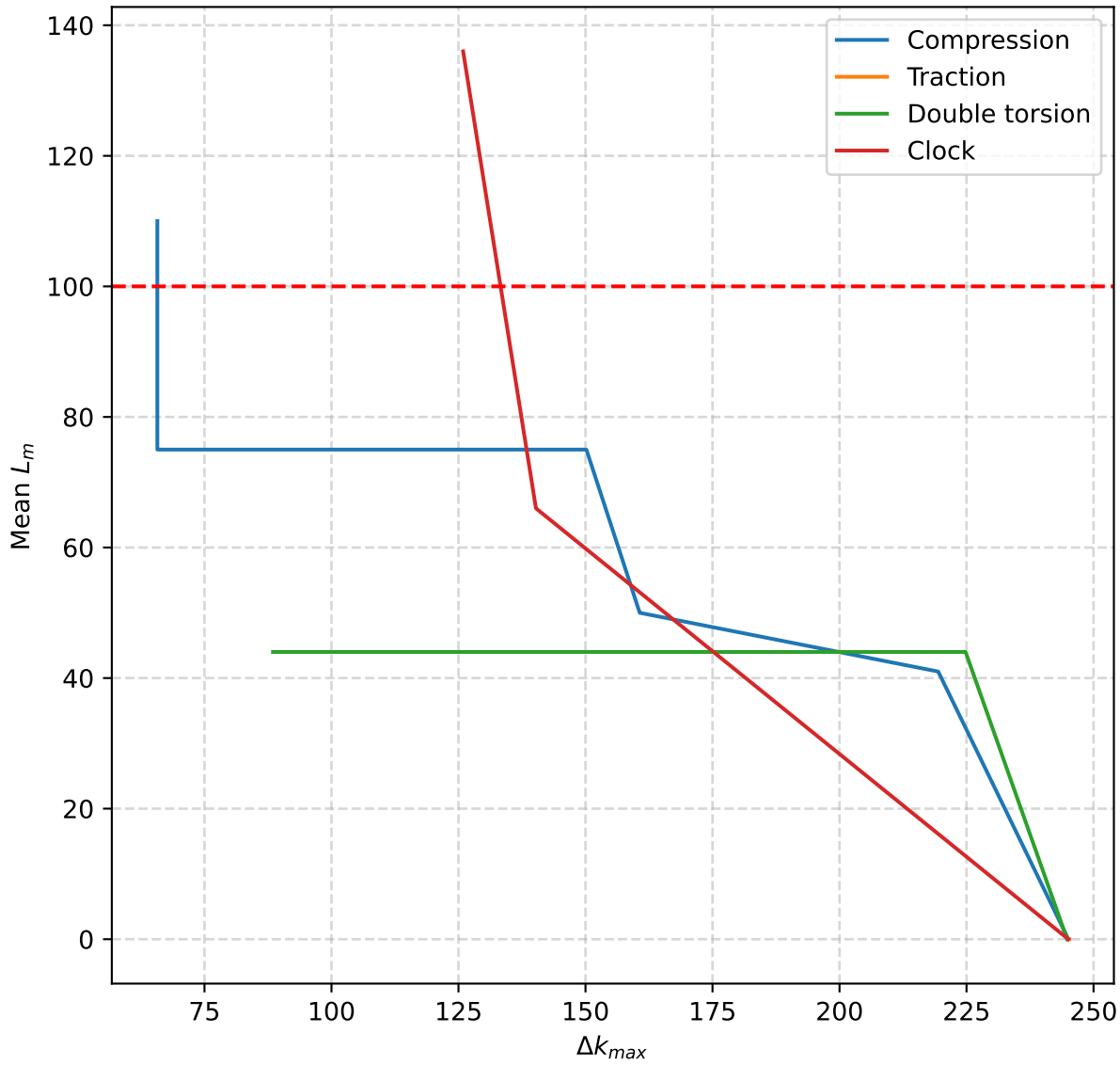


Figure B.3: $L_m$ in function of $\Delta k_{max}$ for all spring families for the adduction movement. Red dashed line : Treshold set for $L_m$

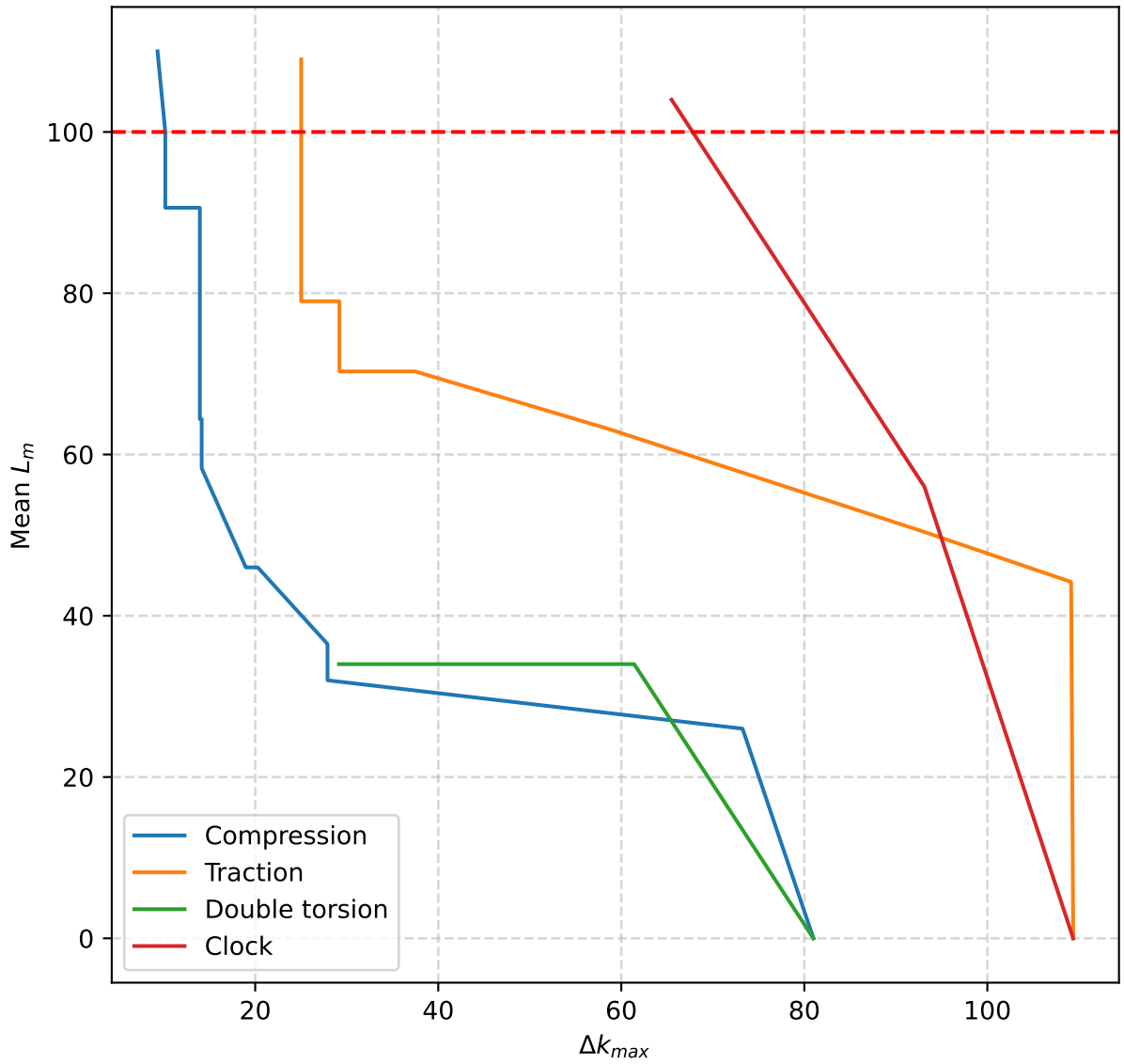


Figure B.4: $L_m$ in function of $\Delta k_{max}$ for all spring families for the abduction movement. Red dashed line : Treshold set for $L_m$

**UNIVERSITÉ CATHOLIQUE DE LOUVAIN**
**École polytechnique de Louvain**
Rue Archimède, 1 bte L6.11.01, 1348 Louvain-la-Neuve, Belgique | **www.uclouvain.be/epl**